The physics of HPM sources

Børve Steinar

Norwegian Defence Research Establishment (FFI)

2008-01-04

FFI-rapport 2008/00014

2008

978-82-464-1316-7

Keywords

High Power Microwaves

Plasma Physics

Radio Frequency Weapons

Non-lethal Weapons

Approved by

Odd Harry Arnesen	Prosjektleder/Project manager
Jan Ivar Botnan	Avdelingssjef/Director

Sammendrag

Mange land har i fleire tiår gjennomført forsking på **høgeffektive mikrobølgjekjelder (HPM)**, både til sivile og militære føremål. Det store gjennombrotet for HPM våpen har derimot lete venta på seg, til trass for at viktige framsteg har blitt gjort. Samstundes vert vi stadig meir avhengig av datastyrte kontrollsystem og trådlause kommunikasjonskanalar, noko som gjer den potensielle gevinsten ved å bruke HPM stadig større. Ein kan difor ikkje seie at forskingsaktiviteten på dette området har sunke dei seinare åra. For betre å kunne vurdere den potensielle faren representert ved HPM våpen og den generelle statusen innan relevant forsking, presenterer vi her ein introduksjon til fysikken bak dei mest vanlege mikrobølgjekjeldene idag. Vi prøver i tillegg å peike på det vi ser på som dei mest lovande teknologiane, sett frå ein militær synsvinkel.

English summary

Many countries have for decades conducted research on **High Power Microwave (HPM)** sources, both for civilian and military purposes. Progress has been made over the years, yet a breakthrough for HPM weaponry is yet to be seen. Still, with an ever increasing dependence on computerized control and wireless communcation systems, the potential gain from applying potent HPM weapons is greater than ever before. There is therefore no observable decline in the research activity in this area. To be able to assess the potential threat from this type of weapons and the current state of related research, we present in this report an introduction to the physical processes utilized in the most common high power microwave sources of today. We also try to point to what we consider, from a military point of view, to be the more promising technologies.

Contents

1 Introduction

Many countries are currently running research projects on **High Power Microwave** sources, both for civilian and military purposes. This applies to countries such as the USA, China, Russia, the Ukraine, Great Britain, Australia, France, Germany, Sweden, South Korea, Taiwan, and Israel [49], to name a few. In 2000, the US Department of Defense (**DoD**) ended the project **High-Power Microwave (HPM) MURI** which had involved 9 universities, 3 private companies, and 3 **DoD** research institutions in a joint effort for 5 years. In its conclusions, the **Air Force Scientific Board** in 1999 wrote [9]:"*Promising present-day research in high-power microwave technology allows us to envision a whole new range of compact weapons that will be highly effective in the sophisticated, electronic battlefield environment of the future*". In a follow-up MURI project that ended in 2005, one focused on technologies critical to producing compact pulsed power generators for driving HPM sources [73]. At the same time, and still ongoing, programs have been run by the 4 separate branches of the armed forces.

Perhaps the only country to match the US research effort on HPM at the moment is China. A large number of scientific papers related to the topic in question has been produced in China over the last 5-10 years. This documents HPM related research in at least 9 universities, most notably the National University on Defense Technologies in Changsha. The focus of the Chinese research has been efficiency enhancment of the MILO and the vircator. In Sweden, **FOI** received a vircator from Texas Tech University in 2003 [30]. After some initial problems with the power generator, the demonstrator got its operational start-up in 2004. The first numerical simulations of the device were documented in 2005 [66]. Results from these simulations fitted qualitatively well with experimental data, although more work on the underlying models was clearly required in order to obtain a better quantitative understanding of the vircator.

FFI has so far focused its activity in this field on evaluating military and civilian equipment, as well as infrastructure on the battle field, with regards to both the well established threat from **Nuclear Electromagnet Pulses (NEMP)** as well as possible threats from newly developed electromagnetic weapons [5]. Testing current and planned equipment on available radiation sources is indeed important. However, it is equally important for the armed forces to be able to assess the current status of research on electromagnetic weapons, and to be able to predict what can be expected from this research both in the near- and mid-term future. This kind of insight is essential in providing updated and relevant threat scenarios. It is of particular importance that the information provided to the armed forces manages to stay ahead of the weapons development. This is because security measures preferably should be taken into account when planning buildings and other long-lived installations [33, 52]. In-depth knowledge of the development in electromagnetic weapons research also offers the armed forces a good basis from which to evaluate whether HPM weapons at some point should be included in ones own strategy for **Less-lethal Weapons**.

As an element in boosting the local expertise on HPM weaponry, we will in this report present an

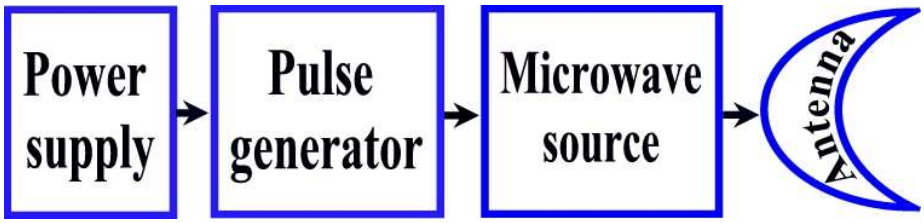

Figure 2.1: General sketch of an HPM weapon.

introduction to the physical processes utilized in the most common high power microwave sources of today. We will also try to assess the current status of the research in this field. Viewing the available technologies more specifically in the light of military needs will be left for a later report. In §2 we sketch features common to many HPM sources and give a brief overview of the various technologies available today for microwave generation. We also take a first look at the equations that we will use later on when trying to understand the physics behind the HPM sources. In §3-8 we take a closer look at the most important classes of HPM source based on the vacuum tube technology, one at the time. In §9 we look at remaining technological challenges and how one foresee these challenges might be overcome. In §10 we discuss briefly to what extent solid-state devices might represent an attractive alternative to vacuum tube devices. Finally, we present a short discussion in §11 on the current state of the HPM research. More specifically, we try to point out what technologies seem to be the more interesting from a military point of view. Appendices A and B provide background information regarding linear wave analysis in plasma physics and Bessel functions, respectively.

2 An HPM weapons overview

A general sketch of an HPM weapon is shown in Figure 2.1. Essential components are: Power supply, pulse generator, microwave source, and antenna.

Power supply/pulsed current generator: HPM sources in general need driver systems that can supply short, intense electrical pulses of 1MV or more for up to $1\mu s$ duration. This can be achieved e.g. through so-called pulse compression or by using capacitor banks that can transform a low-voltage, slowly rising signal into a high-voltage, fast rising signal. One must be careful that the driver system delivers a well-matched signal with regards to voltage and impedance. While conventional microwave sources, such as e.g. radars, typically operate on relatively low voltage and high impedance, the HPM sources will require substantially higher voltage levels and with quite different impedance levels. This has been illustrated in Figure 2.2. A mismatch between the impedance of the driver signal and the HPM source will result in poor energy transfer to the HPM source. This is particularly true if the impedance of the source is lower than the impedance of the driver. The choice of power supply and driver section will therefore largely be by the type of source to be used.

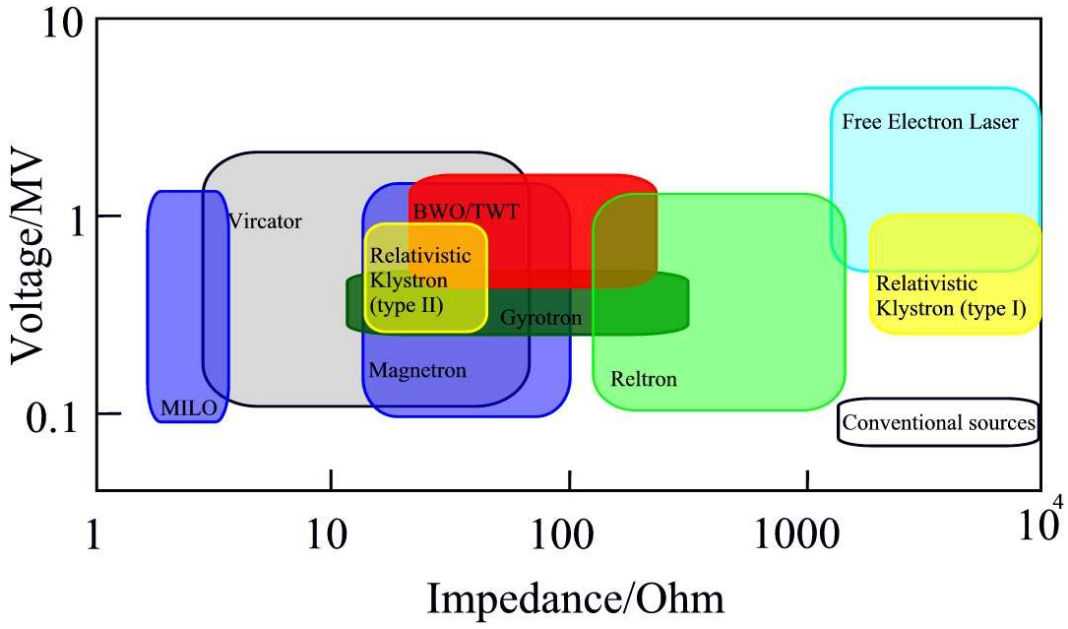

Figure 2.2: Various classes of HPM sources compared with conventional microwave sources with regards to optimal impedance and voltage (derived from [13]).

A common configuration consists of a Marx bank, where a row of capacitors are charged in parallel and then later quickly switched into a series circuit, allowing the voltage to be multiplied by the number of capacitive stages in the Marx. This can serve as an initial current generator for a flux compression generator (FCG). In an FCG a magnetic coil is compressed either by explosive or magnetic forces so that the current level rapidly increases. Another common option is to replace the FCG by a Pulseforming Line (PFL). A third option, used e.g. in the Swedish vircator [30], is to let the electrical pulse for the HPM source be generated directly from a large Marx generator (20-steps Marx generator in the case of the Swedish vircator) charged through a charging aggregate.

Antenna: The antenna should act as the interface between the HPM source and the rest of the world. An HPM source represents a challenge to conventional antenna technology due to the high levels of power and the short pulse lengths. Important properties of an antenna are how well signals can be restricted to propagate in a specific direction and how effective the coupling between the antenna and the surrounding air is. The shape of the antenna can influence to what extend the phenomena known as **air breakdown** is an issue or not while operating at high power levels. This phenomena occurs if the local $\boldsymbol{E}$-field is sufficiently strong. More specifically, the $\boldsymbol{E}$-field needs to transfer enough energy to the electrons so that the atoms in the air becomes ionized after collisions with the high-energy electrons. At the atmospheric pressure level, this occurs at a critical field strength of roughly 24 kV/cm. For pulses with a duration of more than 100ns, ionospheric “plasma mirrors” can be formed at high altitudes which reflect relatively low-frequency microwaves (1GHz). The most common type of antennas for HPM sources are **rectangular horn antenna**. Lately, antenna arrays have presented themselves as promising alternatives.

HPM sources: The basic process behind all vauum tube sources is conversion of kinetic energy in an electron beam into electromagnetic radiation. This conversion is made possible through resonant interactions between the eigenmodes of cavities and/or waveguides and the natural oscillation modes in an electron plasma. Sources are organized in several ways, depending on what properties are focused on: By dividing sources into **fast-** and **slow-wave** devices, one separate those cases where the eigenmodes of the waveguide have phase velocities that are either larger or smaller, respectively, than the sound speed. In the former case, the radiation is generated by having electrons pass either from one medium to another, where the two media have different refraction index, or through perturbations in the medium such as a grid or a perforated plate. In the case of a slow-wave device, so-called **Cerenkov radiation** is produced when the electrons move faster than the phase velocity of the electromagnetic waves. As an alternative strategy for organizing radiation sources, one separates sources into the 3 categories **O-** and **M-type** and **space charge type**. In the first case, electrons move parallel to a strong magnetic field. In the second case, one utilizes the fact that charged particles will experience a drift normal to $\boldsymbol{E}$ and $\boldsymbol{B}$ when these two fields are not parallel. The last case is based on the formation of so-called **virtual cathodes** when the current exceeds the space-charge limit. An external magnetic field is not strictly necessary in this case.

2.1 Basic equations

The different types of HPM sources listed above all base the generation of radiation in one way or another on the interaction between a relativistic electron beam and an electromagnetic wave field. The dynamics of the wave field is described by Maxwell's equations:

$$\nabla \times \boldsymbol{E} = -\frac{\partial \boldsymbol{B}}{\partial t} \qquad \textit{(Faraday's law)} \tag{2.1}$$

$$\frac{1}{\mu_0}\nabla \times \boldsymbol{B} = \boldsymbol{J} + \epsilon_0 \frac{\partial \boldsymbol{E}}{\partial t} \qquad \textit{(Ampére-Maxwell's law)} \tag{2.2}$$

$$\nabla \cdot \boldsymbol{E} = \frac{\rho}{\epsilon_0} \qquad \textit{(Poisson's law)} \tag{2.3}$$

$$\nabla \cdot \boldsymbol{B} = 0 \qquad \textit{(Gauss's law)}, \tag{2.4}$$

where $\boldsymbol{E}$ and $\boldsymbol{B}$ are electric og magnetic field strengths, $\boldsymbol{J} = \rho \boldsymbol{v}$ is the current vector, ρ is the charge density, and ϵ_0 and μ_0 are the permittivity and permeability in vacuum. Often when referring to the magnitude of the current vector, I is used instead of J. It is also sometimes favourable to use formulations based on the electric scalar potential, ϕ, and the magnetic vector potential, $\boldsymbol{A}$, instead of $\boldsymbol{E}$- and $\boldsymbol{B}$-fields directly. The expressions coupling fields and potentials are

$$\boldsymbol{B} = \nabla \times \boldsymbol{A} \tag{2.5}$$

and

$$\boldsymbol{E} = -\nabla\phi - \frac{\partial \boldsymbol{A}}{\partial t}. \tag{2.6}$$

The vector potential, and thus also the magnetic field, is negligible in the electrostatic limit. By combining equations 2.1-2.4 we can obtain the wave equations for the $\boldsymbol{E}$- and $\boldsymbol{B}$-fields:

$$\nabla^2 \boldsymbol{E} - \frac{1}{c^2}\frac{\partial^2 \boldsymbol{E}}{\partial t^2} = \frac{\nabla \rho}{\epsilon_0} + \mu_0 \frac{\partial \boldsymbol{J}}{\partial t} \tag{2.7}$$

and

$$\boldsymbol{\nabla}^2\boldsymbol{B} - \frac{1}{c^2}\frac{\partial^2\boldsymbol{B}}{\partial t^2} = -\mu_0\boldsymbol{\nabla}\times\boldsymbol{J}, \tag{2.8}$$

where $c^{-2} = \epsilon_0\mu_0$. In vacuum, the right hand sides in equations 2.7 and 2.8 equal 0. Important special cases in cylindrical and rectangular symmetry are the transverse magnetic modes (TM-modes) and the transverse electric modes (TE-modes). In the former case the axial magnetic field is zero, while in the latter case the axial electric field is zero.

In addition, we need equations to describe the electron dynamics. First, we need the continuity equation. Assuming we can neglect sinks or sources of particles, the continuity equation can be formulated as

$$\frac{\partial\rho}{\partial t} + \boldsymbol{\nabla}\cdot\boldsymbol{J} = 0. \tag{2.9}$$

If we also assume the electrons to only be under influence of electromagnetic forces, the momentum equation becomes

$$\frac{\partial\boldsymbol{p}}{\partial t} + (\boldsymbol{v}\cdot\boldsymbol{\nabla})\boldsymbol{p} = -e(\boldsymbol{E} + \boldsymbol{v}\times\boldsymbol{B}), \tag{2.10}$$

where $\boldsymbol{p} = \gamma m_e\boldsymbol{v}$ and

$$\gamma(v) = 1/\sqrt{1 - v^2/c^2} = 1/\sqrt{1-\beta^2}. \tag{2.11}$$

is the relativistic mass factor. The mass m_e will always refer to the rest mass of the electrons. If the motion of the electrons is one-dimensional (in the chosen representation), equation 2.10 can easily be rewritten so that $\boldsymbol{p}$ does not explicitly enter in the expression. To achieve this, we use the relation

$$\frac{\partial p}{\partial x} = \frac{\partial p}{\partial v}\frac{\partial v}{\partial x} = m\left(\gamma^3\frac{v}{c^2}v + \gamma\right)\frac{\partial v}{\partial x} = m\gamma^3\frac{\partial v}{\partial x}. \tag{2.12}$$

Applied to the momentum equation 2.10 in the direction parallel to $\boldsymbol{v}$, this produces the following equation

$$\left(\frac{\partial\boldsymbol{v}}{\partial t}\right)_{\parallel} + (\boldsymbol{v}\cdot\boldsymbol{\nabla})\boldsymbol{v} = -\frac{e}{m_e\gamma^3}\boldsymbol{E}_{\parallel}. \tag{2.13}$$

Note that the magnetic force is absent altogether from equation 2.13 since this force always is normal to $\boldsymbol{v}$.

2.2 Fundamental electron plasma behaviour

To fully understand the results on wave excitation presented in this report, it is vital that the reader has some understanding of fundamental characteristics of the interaction between electrons and an electromagnetic field. In the present context we will restrict the discussion to deriving two important plasma parameters, namely the plasma (ω_p) and cyclotron (ω_c) frequencies.

In the case of the former parameter, we look at a purely electrostatic problem where the system can be described by equations 2.3, 2.9, and 2.10. We apply the technique of **small-amplitude analysis** described in appendix A to this system, with the additional assumption that the equilibrium solution is uniform with no flow present. (This requires the presence of another uniformly distributed,

positively charged, and static plasma population that secures charge neutrality in the equilibrium solution.) First we take the divergence of the momentum equation, equation 2.10, and use the Poisson's law, equation 2.3, to eliminate the dependence on $\boldsymbol{E}$. The resulting expression for $\boldsymbol{\nabla} \cdot \boldsymbol{v}$ can be combined with the continuity equation, assuming we have taken the time-derivative of the latter equation first. We then end up with the following second-order differential equation for the electron density:

$$\frac{\partial^2 \delta\rho}{\partial t^2} - \omega_p^2 \delta\rho = 0, \tag{2.14}$$

where

$$\omega_p = -\frac{e\rho_0}{\epsilon_0 m} = \frac{e^2 n_0}{\epsilon_0 m} \tag{2.15}$$

is the nonrelativistic plasma frequency.

The second plasma parameter to be derived in this section, the cyclotron frequency, is related to the motion of isolated electrons in a uniform magnetic field, $\boldsymbol{B}$. Since the magnetic force, $-e\boldsymbol{v} \times \boldsymbol{B}$, always is normal to the velocity $\boldsymbol{v}$, an electron will undergo a circular motion with constant angular velocity. In general, the relation between the angular velocity, denoted here by ω_c, and the centriple force, in this case identical to the magnetic force, is

$$m\omega_c^2 r = evB_\perp = e\omega_c r B_\perp. \tag{2.16}$$

The nonrelativistic cyclotron frequency is therefore given as

$$\omega_c = \frac{eB_\perp}{m}. \tag{2.17}$$

3 Klystrons

This is a fast-wave device of type O. Sources of this category are known to produce high output power, have relatively broad bandwidths, be highly efficient compared to other HPM sources (efficiency of around $40 - 60\%$ common), and be highly stable with regards to phase and amplitude. However, the pulse lengths are typically short, typically around 100ns. The interaction between the electrons and the waves occurs at specific locations along the path of the electron beam where the resonant cavities are placed. The microwave signal is elsewhere transported by the electron beam through perturbations in the space charge density (so-called clumping).

3.1 Non-relativistic velocity modulation

To provide insight into the fundamental principles of klystrons, we will present a simplified, non-relativistic model of a klystron-like, two-cavity source [8, 83]. Let us assume the electron beam is

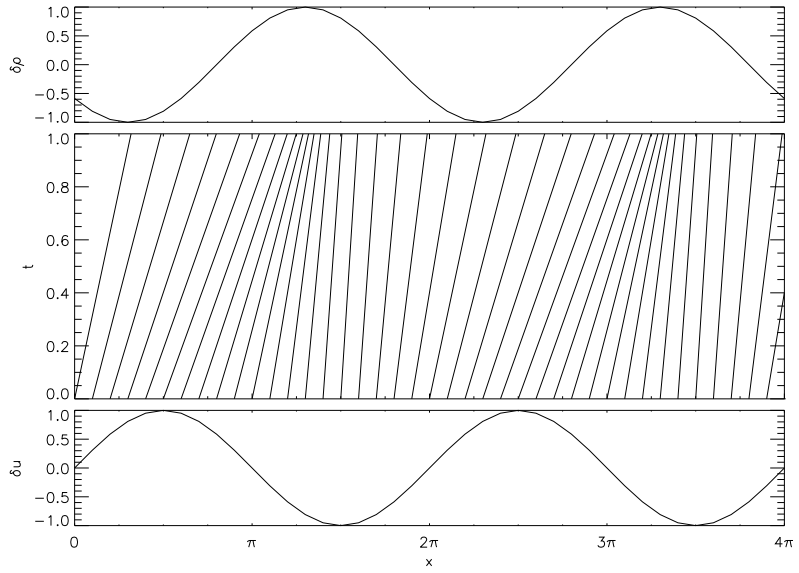

Figure 3.1: Periodic modulation of the electron velocity (bottom graph) is over time shown in the Applegate diagram to result in a corresponding, phase shifted, density modulation (top graph). This is a simple consequence of the continuity equation 2.9 for a compressible fluid.

initially accelerated by the electric potential V_0. The velocity of the electrons before entering the first cavity is found by applying the principle of energy conservation as

$$v_0 = \sqrt{\frac{2eV_0}{m}}. \tag{3.1}$$

The electric current corresponding to the electron beam is $I_0 = en_0v_0$, where e is the charge of an electron and n_0 is the density of the incoming beam. Clumping of the electron beam is achieved by applying an oscillating potential across a pair of grids connected to the first cavity. Let the electric potential be given as $V_1 = \alpha V_0 \sin(\omega t)$, where $\alpha < 1$. If the variation of the potential is sufficiently slow, the individual electrons will experience a more or less constant potential as they pass through the region between the grids. Some electrons will experience an accelerating field, while others will experience a retarding field. Beyond the second grid, the velocity of the electron beam, v_1, will vary in time as

$$v_1(t) = v_0\sqrt{1+\alpha\sin(\omega t)} \approx v_0\left[1+\frac{\alpha}{2}\sin(\omega t)\right], \tag{3.2}$$

where t refers to the time for passing through the first cavity. The electric current after the first cavity is correspondingly $I_1 = I_0\sqrt{1+\alpha\sin(\omega t)} \approx I_0$. If we neglect the internal forces in the plasma, the velocity of a given electron will stay constant after passing through the first cavity. As illustrated by the so-called **Applegate**-diagram (figure 3.1), a periodic modulation of the electron density is produced as a consequence of the perturbation in velocity.

The time interval spent by a given electron in covering the distance s between the two cavities is given as

$$T(t) = \frac{s}{v_1(t)} \approx sv_0\left[1-\frac{\alpha}{2}\sin(\omega t)\right]. \tag{3.3}$$

Due to this time-varying delay, the electric current near the second cavity, I_2, will exhibit a stronger variability than I_1. We find I_2 by recalling the definition of electric current:

$$I_2(t) = \frac{dq}{dt'}, \tag{3.4}$$

where q is the charge and $t' = t + T(t)$ is the time for passing through the second cavity. Differentiation produces $dt' = dt + dT(t) = dt(1 + dT(t)/dt)$. From charge conservation we have $I_0 dt = I_2(t)(dt + dT(t))$, and by differentiating $T(t)$ we can obtain an expression for I_2:

$$\begin{aligned} I_2(t) &= I_0\left(1 + \frac{dT}{dt}\right)^{-1} && (3.5)\\ &\Updownarrow && (3.6)\\ I_2(t) &= \frac{I_0}{1 - X\cos(\omega t)} && (3.7) \end{aligned}$$

where we have defined

$$X = \frac{\alpha}{2}\theta_0 \equiv \frac{s\omega\alpha}{2v_0}, \tag{3.8}$$

known as the "bunching parameter". Using Fourier expansion and the notations $\phi \equiv \omega t$ and $\phi' \equiv \omega t'$ we can rewrite $I_2(t)$ as

$$I_2(t) = I_0 + \sum_{n=1}^{\infty}[a_n \cos(\phi' - \theta_0) + b_n \sin(\phi' - \theta_0)] \tag{3.9}$$

where the coefficients are

$$a_n = \frac{1}{\pi}\int_{\theta_0-\pi}^{\theta_0+\pi} I_2(t)\cos[n(\phi' - \theta_0)]d\phi' = \frac{I_0}{\pi}\int_{\pi}^{\pi}\cos[n(\phi - X\sin\phi)]d\phi = 2I_0 J_n(nX) \tag{3.10}$$

and

$$b_n = \frac{1}{\pi}\int_{\theta_0-\pi}^{\theta_0+\pi} I_2(t)\sin[n(\phi' - \theta_0)]d\phi' = \frac{I_0}{\pi}\int_{\pi}^{\pi}\sin[n(\phi - X\sin\phi)]d\phi = 0. \tag{3.11}$$

The function $J_n(x)$ is the Bessel function of order n (see appendix B). In figure 3.2, the current at the second cavity, $I_2(t)$, is plotted for three different values of X. When $X > 1$, ϕ' is a multivalued function of ϕ leading to electron overtaking.

If an electric potential is applied to the second cavity similarly to that of the first cavity with a maximum amplitude of V_0, it is possible to transfer energy *from* the electrons *to* the wave field. To achieve a net increase in the electromagnetic field strength, the field in the cavity must decelerate the electrons when the current density is at its strongest, and similarly, accelerate the electrons when the current density is at its weakest. We will estimate the output power from this configuration when only the fundamental harmonic ($n = 1$) is considered. In this case $I_2(t) = I_0[1 + 2J_1(X)\cos(\phi - \theta_0)]$, where the maximum value of $J_1(X)$ is roughly 0.58 occuring at $X = 1.8$. The time-averaged power output will then be

$$P_{\text{out}} = \frac{1.16 I_0}{\sqrt{2}}\frac{V_0}{\sqrt{2}} = 0.58 P_{\text{in}}. \tag{3.12}$$

In other words, this configuration represents a maximum of 58% efficiency in power conversion.

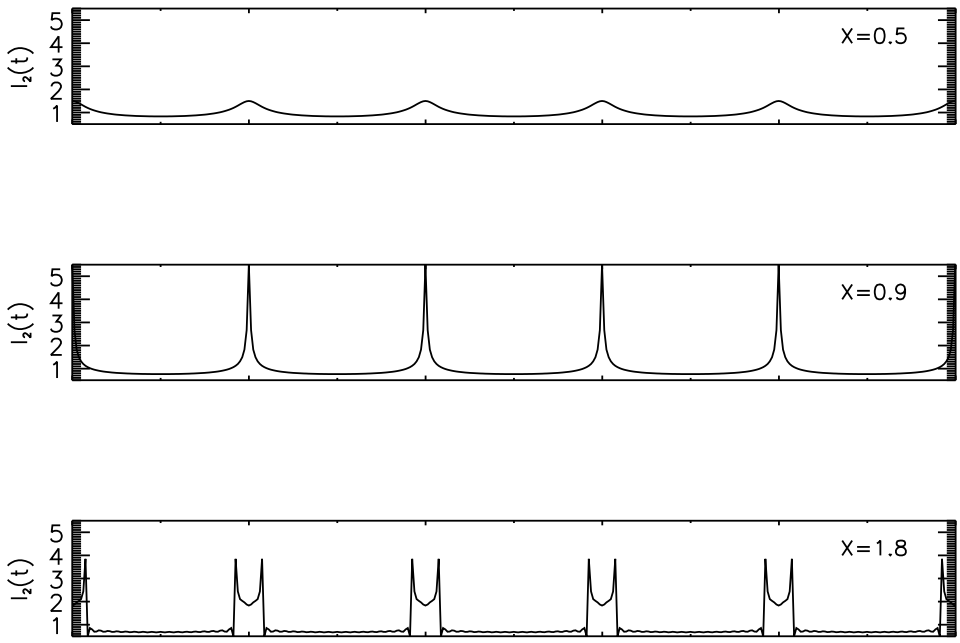

Figure 3.2: Current at the second cavity, I_2, plotted as a function of time for three different values of the "bunching parameter", X.

3.2 Space-charge wave theory

In the previous section we looked at electron bunching through velocity modulation. Throughout that discussion we neglected effects due to self-interaction, how the electron dynamics is influenced by the electric field produced by the electrons themselves. In this section we will investigate how small-signal space-charge waves modify the output current. This is normally done in a linear wave analysis where one assumes that the waves are small corrections to an otherwise equilibrium state. In this particular problem we also apply the following assumptions: (1) Fluid velocities are sufficiently small so that relativistic and self-consistent magnetic field effects can be neglected. (2) All equilibrium solutions are uniform. (3) Wave propagation and particle dynamics is restricted to the z-direction. (4) Wave amplitudes are only allowed to vary perpendicular to the z-axis.

The technique of linear wave analysis, with the exact same assumptions listed above, is demonstrated in appendix A. Therefore, we only reproduce the results for the parallel component of the electric field, δE_z, as stated by expression A.9:

$$\boldsymbol{\nabla}_\perp^2 \delta E_z - T^2 \delta E_z = 0, \tag{3.13}$$

where

$$T = \left\{ (k^2 - K^2) \left[1 - \frac{\omega_p^2}{(\omega - v_{0z}k)^2} \right] \right\}^{1/2}, \tag{3.14}$$

$\boldsymbol{\nabla}_\perp$ is the perpendicular component of the gradient vector, ω is the angular frequency of the wave, k is the wavenumber, $K = \omega/c$ is the free space wavenumber, and $\omega_p = \sqrt{e^2 n_0/(\epsilon_0 m)}$ is the electron plasma frequency. If no transverse variation is allowed, that is $\boldsymbol{\nabla}_\perp^2 \delta E_z = 0$, then $T = 0$. The 4 solutions to this equality comprise a pair of plane free space waves,

$$k_{1,2} = \pm K, \tag{3.15}$$

and a pair of plasma waves with propagation speeds either above or below the beam velocity,

$$k_{3,4} = \frac{\omega \pm \omega_p}{v_{0z}}. \tag{3.16}$$

For a given solution, k_n, all variables in this analysis are expressed on the form given in equation A.1. The total solution is a linear combination of all the solutions. For the velocity perturbation, we can write it as

$$\frac{\delta v_z}{v_{0z}} = \sum_{n=1}^{n=4} \Lambda_n e^{ik_n z}, \tag{3.17}$$

where we eliminated the temporal term $\exp(-i\omega t)$. By combining equations 3.17, A.7, and A.8, the following expression is obtained for the total current perturbation

$$\frac{\delta J_z}{J_{0z}} = \sum_{n=1}^{n=4} \frac{\omega}{\omega - k_n v_{0z}} \Lambda_n e^{ik_n z}. \tag{3.18}$$

At $z = 0$, right after the "buncher" cavity, the relative amplitude of the velocity perturbation is given roughly by equation 3.2 as $\alpha/2$, whereas the current perturbation at this point in space is negligible. From this we can conclude that

$$\sum_{n=1}^{n=4} \Lambda_n = \frac{\alpha}{2} \tag{3.19}$$

and

$$\sum_{n=1}^{n=4} \frac{\omega}{\omega - k_n v_{0z}} \Lambda_n = 0 \tag{3.20}$$

which implies that

$$\Lambda_1 = \Lambda_2 = 0 \tag{3.21}$$

and

$$\Lambda_3 = \Lambda_4 = \frac{\alpha}{4}. \tag{3.22}$$

Inserting this into expression 3.18 for δJ_z yields

$$\frac{\delta J_z}{J_{0z}} = \frac{\alpha}{4}\frac{\omega}{\omega_p}\left[-e^{i\omega_p z/v_{0z}} + e^{-i\omega_p z/v_{0z}}\right] e^{i\omega z/v_{0z}} = -i\frac{\alpha}{2}\frac{\omega}{\omega_p}\sin(\omega_p z/v_{0z}) e^{i\omega z/v_{0z}}. \tag{3.23}$$

If one were to solve the more realistic problem of a finite sized beam with radius r_b in a cylindrical waveguide with radius $r_w \geq r_b$, a very similar result would be obtained. The resulting expression for the current perturbation would be identical to equation 3.23, with the exception that the ratio ω/ω_p would be replaced by ω/ω_q, where ω_q/ω_p is dependent on $\omega r_b/v_{0z}$ and r_w/r_b [8]. In section 3.4 we will consider the related problem of finding the dispersion relation for an annular, relativistic beam in a cylindrical waveguide.

3.3 Relativistic Klystron

Type 1 (SLAC) Relativistic Klystron Amplifier (RKA) [3] is based on a purely relativistic extrapolation of the conventional klystron technology. The cross-section of the electron beam is a solid circle, and a relatively high number of resonance cavities are used. The electrons are strongly relativistic with energies well above 1MeV. The current density, on the other hand, is quite moderate (less than 1kA), which implies an impedance of over 1000Ω. The power of the resulting radiation has been reported to be roughly 300MW in the X-band.

Type 2 (NRL) RKA [55] distinguishes itself from type 1 by utilizing an annular electron beam with dominant space charge effects and normally only 3 cavities. This makes it possible to produce anomalous, harmonic-rich currents with large-scale clumping. Unfortunately, this clumping also leads to reduced efficiency in converting electron beam modulations into microwave radiation. Still, effects up to 10GW in the L-band have been reported.

Relativistic Klystron Oscillator (RKO): Part of the electron beam can be reflected back from the second to the first cavity [78]. This occurs if the voltage across cavity 2 is large enough so that a virtual cathode is formed there, or if the two cavities are positioned close enough so that a pure

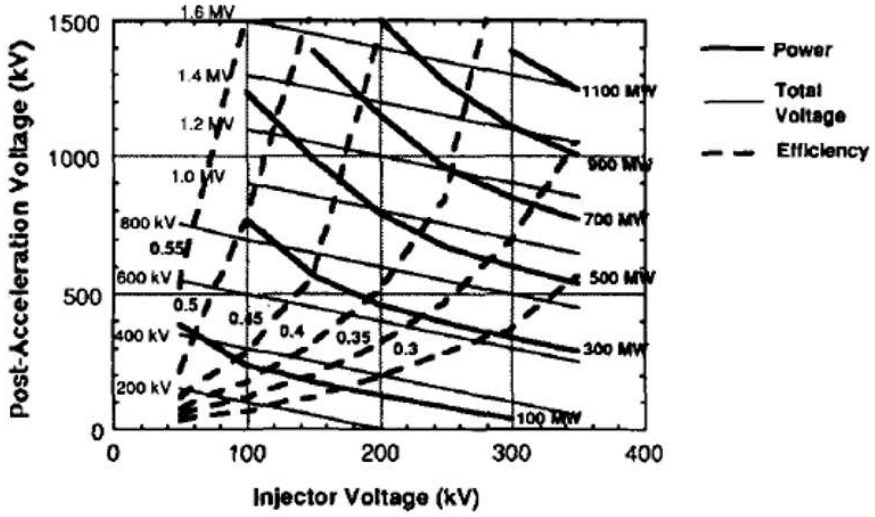

Figure 3.3: Constant power, efficiency and total voltage level in a Reltron as a function of the injection and acceleration voltage [60].

electromagnetic coupling between the two exists. In this case, the reflected electron beam can contribute to further excitation. This is only achieved if the return current is in-phase with the original excitation in cavity 1.

Reltron: This is a relative new addition to the klystron family originally developed with reliable and cost-efficient susceptibility tests in mind [59]. Today, this concept represents one the best alternatives for narrow-band radiation sources when it comes to power per volume and power per mass. Specific energies per pulse of about 2.6 J/kg [9] and efficiency numbers upto 50% were reported already around 1998 [61]. The experimental models have reported peak power levels of around 600MW, while the commercial models promise about half of that. The length and diameter of an L-band reltron is reported to be 75cm and 40cm, respectively, while the weight is less than 100kg. Experiments with a miniturized version of the Reltron having a diameter of less than 8cm, have also been conducted [23]. It is thus one of the most interesting concepts from a military viewpoint. Sources of this kind exhibit in addition great stability and flexibility when it comes to output frequency. What distinguishes the Reltron from other klystron-type sources, is the way the electron beam undergo a second acceleration phase after being injected into the vacuum tube and having gone through a klystron-like bunching phase. In the second acceleration phase, the electrons reach relativistic velocities. At the same time, the energy spread in the beam is reduced. As shown in figure 3.3 (taken from [60]), the output power will depend on the voltage in both the injection level and the acceleration level, as well as the mean current and efficiency.

3.4 Properties of an annular, relativistic electron beam

Most common types of klystron-like radiation sources today use an annular electron beam. Therefore, we will take a closer look at the properties of such beams in the relativistic regime, with a particular attention given to space-charge effects that will affect the output power of the generated radiation [19, 22]. Let us assume an infinitely thin, annular beam with radius r_b inside a pipe-shaped waveguide with radius r_w. The electrons have initially been accelerated by the electric potential $\phi_{inj} < 0$ relative to the cavity walls. The electric potential in the waveguide is found using the Poisson equation on integral form as

$$\oint_S \boldsymbol{E} \cdot \boldsymbol{ds} = \Delta Q/\epsilon_0, \tag{3.24}$$

where S is a pipe-shaped shell with radius r ($r_b \leq r < r_w$). The charge ΔQ equals the total charge in a ΔL long section of the beam. Expressed in terms of the current I and the electron velocity v, the charge becomes $\Delta Q = \Delta L I/v$. The given charge distribution is consistent with a purely radially directed $\boldsymbol{E}$ field, which based on equation 3.24 becomes

$$E_r(r,z) = \frac{I(z)}{2\pi\epsilon_0 v(z) r}, \;\; r \geq r_b. \tag{3.25}$$

For $r < r_b$ we have $E_r(r,z) = 0$. The electric potential $\phi(z)$, relative to the potential on the waveguide wall, is found to be

$$\phi(r,z) = -\int_r^{r_w} E_r(r,z)dr = \frac{I(z)}{2\pi\epsilon_0 v(z)} \ln\left(\frac{r}{r_w}\right), \;\; r_b \leq r \leq r_w. \tag{3.26}$$

Since $E_r = 0$ for $r < r_b$, then $\phi(r,z) = \phi(r_b,z) \equiv \phi_b(z)$ for $r < r_b$.

After the initial acceleration, the kinetic energy of the electrons will be

$$E_K \equiv (\gamma_{inj} - 1)mc^2 = -e\phi_{inj}, \tag{3.27}$$

where $\gamma_{inj} = \gamma(v_{inj})$ is the relativistic mass factor at injection. As the electron beam passes into the waveguide, some of the kinetic energy is transformed into potential energy. From the principle of energy conservation, we have

$$m_0c^2\gamma_{inj} = m_0c^2\gamma_0 - e\phi_b, \tag{3.28}$$

where $\gamma_0 = \gamma(v_0)$. By combining equations 3.26 and 3.28 with the definition of γ, the equilibrium current in the electron beam, I_0, can be written as

$$I_0(\gamma_0) = I_s\sqrt{\gamma_0^2 - 1}\frac{\gamma_{inj} - \gamma_0}{\gamma_0}, \tag{3.29}$$

where

$$I_s = \frac{2\pi\epsilon_0 m_0 c^3}{e\ln(r_w/r_b)} = \frac{8.5\text{kA}}{\ln(r_w/r_b)}. \tag{3.30}$$

By differentiating I_0 with respect to γ_0, the maximum stationary current achievable in a given waveguide can be found:

$$\frac{dI_0}{d\gamma_0} = 0 \tag{3.31}$$

$$\Updownarrow \tag{3.32}$$

$$I_s \frac{\gamma_{inj} - \gamma_0^3}{\gamma_0^2\sqrt{\gamma_0^2 - 1}} = 0 \tag{3.33}$$

$$\Updownarrow \tag{3.34}$$

$$\gamma_0 = \gamma_{inj}^{1/3}. \tag{3.35}$$

This corresponds to a maximum current I_c given as

$$I_c = I_0(\gamma_0 = \gamma_{inj}^{1/3}) = I_s(\gamma_{inj}^{2/3} - 1)^{3/2}, \tag{3.36}$$

which represents an upper theoretical limit for the current. The ratio of kinetic energy to potential energy in this case is

$$\frac{E_K}{E_P} = \frac{\gamma_{inj}^{1/3} - 1}{\gamma_{inj} - \gamma_{inj}^{1/3}} \leq \frac{1}{2}. \tag{3.37}$$

The potential energy will in other words dominate over the kinetic energy, particularly if $\gamma_{inj} \to 0$, that is in the strongly relativistic case. These are properties that clearly inhibit an efficient microwave generation. To maximize I_c for a given γ_{inj}, it is common to increase r_b and let $r_w/r_b \approx 1$. Near cavities, where r_w effectively increases, I_c will be reduced. At the same time, the current will start to oscillate due to the velocity modulation at the "buncher" cavity. As a consequence, the current can locally exceed I_c, which in turn will lead to a strong modulation of the electron beam.

3.4.1 Dispersion relation

We will derive the dispersion relation for the configuration described in section 3.4 [54], and we will restrict ourselves to TM_{0p}-modes where only δE_r, δE_z, and δB_θ are nonzero. We once again follow the approach outlined in appendix A. In this case, it is appropriate to look for a vacuum solution, which will be valid for $r \neq r_b$. With $\omega_p = 0$, equation A.9 simply becomes

$$\boldsymbol{\nabla}_\perp^2 \delta E_z + (K^2 - k^2)\delta E_z = 0, \tag{3.38}$$

where $K = \omega/c$. To simplify the notation further, we define $\Gamma^2 = K^2 - k^2$. Due to the cylinder symmetry, equation 3.38 can be rewritten as

$$r^2 \frac{\partial^2 \delta E_z}{\partial r^2} + r\frac{\partial \delta E_z}{\partial r} + \Gamma^2 r^2 \delta E_z = 0, \tag{3.39}$$

which from consulting appendix B is easily identified as the **Bessel equation of zeroth order** with Γr as the variable. Since δE_z should be finite for all values of r, including $r = 0$, the general solutions can be written as

$$\delta E_z = \begin{cases} AJ_0(\Gamma r) & 0 \leq r \leq r_b \\ BJ_0(\Gamma r) + CY_0(\Gamma r) & r_b < r < r_w. \end{cases} \tag{3.40}$$

By combining the azimuthal component of Faraday's law, equation 2.1, with the axial component of Ampére-Maxwell's law, equation 2.2, δE_r can be expressed as

$$\delta E_r = \frac{ik}{\Gamma^2}\frac{d\delta E_z}{dr}. \tag{3.41}$$

By further utilizing property B.7, the general solution for the radial component of the electric field is

$$\delta E_r = -\frac{ik}{\Gamma}\begin{cases} AJ_1(\Gamma r) & 0 \leq r \leq r_b \\ BJ_1(\Gamma r) + CY_1(\Gamma r) & r_b < r < r_w. \end{cases} \tag{3.42}$$

To determine the coefficients A, B, and C, we have to consider restrictions put on the solution at $r = r_b$ and $r = r_w$. Continuity of δE_z at $r = r_b$ requires

$$A = B + C\frac{Y_0(\Gamma r_b)}{J_0(\Gamma r_b)}. \tag{3.43}$$

By assuming perfectly conducting wave guide walls, implying $\delta E_z(r = r_w) = 0$, we get

$$BJ_0(\Gamma r_w) + CY_0(\Gamma r_w) = 0. \tag{3.44}$$

The last requirement the solution should meet comes from the integral form of Poisson's law, equation 2.3, which can be written as

$$\epsilon_0 \oint_{\delta S} \delta \boldsymbol{E} \cdot \boldsymbol{ds} = \oint_{\delta V} \delta\rho dV \tag{3.45}$$

where δV is an infinitely long, cylindrical shell with radial extension $[r_b^+, r_b^-] \equiv [r_b - \delta r, r_b + \delta r]$. Taking the geometry into account, we can rewrite equation 3.45 as

$$\epsilon_0(\delta E_r(r_b^+) - \delta E_r(r_b^-)) = \int_{r_b^-}^{r_b^+} \rho r dr. \tag{3.46}$$

To be able to express $\delta\rho$ in terms of δE_z evaluated at $r = r_b$, we utilize equation A.7 derived in appendix A,

$$\delta\rho = \frac{ik\epsilon_0\omega_p^2}{\gamma_0^3(\omega - v_{0z}k)^2}\delta E_z(r_b)\delta(r_b - r), \tag{3.47}$$

with the exception that we include the relativistic factor γ_0^3 that originates from the relativistic momentum equation, equation 2.13. By putting equation 3.47 into 3.45 and utilizing that

$$\int_{r_b^-}^{r_b^+} r\delta(r_b - r)dr = r_b \tag{3.48}$$

we get

$$\delta E_r(r_b^+) - \delta E_r(r_b^-) = \frac{ik\omega_p^2}{\gamma_0^3(\omega - v_{0z}k)^2}\delta E_z(r_b). \tag{3.49}$$

Expressions 3.40 and 3.42 can then replace δE_z and δE_r, respectively, in equation 3.49 to produce the relation

$$-\frac{ik}{\Gamma}[BJ_1(\Gamma r_b) + CY_1(\Gamma r_b) - AJ_1(\Gamma r_b)] = \frac{ik\omega_p^2}{\gamma_0^3(\omega - v_{0z}k)^2}AJ_0(\Gamma r_b). \tag{3.50}$$

A dispersion relation is now found by looking for a nontrivial solution of equations 3.43, 3.44, and 3.50. These three equations, in combination with property B.8 of the Bessel functions, result in the following dispersion relation for an annular, relativistic electron beam:

$$(\omega - v_{0z}k)^2 = \alpha(k^2c^2 - \omega^2)R \equiv \alpha_R(k^2c^2 - \omega^2). \tag{3.51}$$

To simplify the expression we have introduced the parameters

$$\alpha = \frac{\omega_p^2}{r_b\gamma^3}\frac{r_b^2}{c^2}\ln\left(\frac{r_w}{r_b}\right) = \frac{I_0}{I_s\gamma_0^3\beta_0}, \tag{3.52}$$

which depends on the initial conditions of the electron beam, and

$$R = -\frac{\pi/2}{\ln(r_b/r_w)}\frac{J_0(\Gamma r_b)}{J_0(\Gamma r_w)}[Y_0(\Gamma r_w)J_0(\Gamma r_b) - J_0(\Gamma r_w)Y_0(\Gamma r_b)]. \tag{3.53}$$

, which is known as the **reduction factor** and depends on the waveguide geometry. Note that if $J_0(\Gamma r_w) = 0$ then R becomes infinite, indicating resonance with the natural waveguide modes. If we assume that $R \approx 1$, we can solve equation 3.51 to obtain

$$\omega = \frac{v_{0z}k}{1+\alpha}(1 \pm \alpha\mu), \tag{3.54}$$

where

$$\alpha\mu = \frac{\sqrt{\alpha^2 + \alpha/\gamma_0^2}}{\beta_0}. \tag{3.55}$$

The two solutions are typically referred to as the slow $(-)$ and fast $(+)$ wave solutions.

4 O-type Cerenkov devices

An electron moving through a dielectric material with permittivity equal to ϵ will emit **Cerenkov radiation** if the speed exceeds the local speed of light, $c_r = c\sqrt{\epsilon_0/\epsilon}$, where c and ϵ_0 are the speed of light and permittivity in vacuum, respectively. In the resonator of the microwave source, c_r equals the phase speed of the resonant normal mode parallel to the electron beam. A so-called **slow-wave structure (SWS)** is used to reduce the local speed of light. This is typically a periodic, e. g. sinusoidal, modulation of the waveguide walls. According to the boundary conditions, the $\boldsymbol{E}$- and $\boldsymbol{B}$-fields should reflect any wall modulation. The microwave radiation is generated through an interaction between the structure modes and the slow space charge waves. Figure 4.1 shows schematically the interaction between a cavity with modulation period d and four different sources of this type in a dispersion diagram. The two solid lines correspond to $\omega = kc$, while the dotted, dashed, and dash-dotted lines indicate the dispersion relation for three different electron beam velocities. The triangles mark resonances utilized in four different radiation sources.

Conventional versions of **Backward Wave Oscillator (BWO)** and **Travelling-Wave Tube (TWT)** were invented as early as during the second world war, and the first genuine HPM source to be

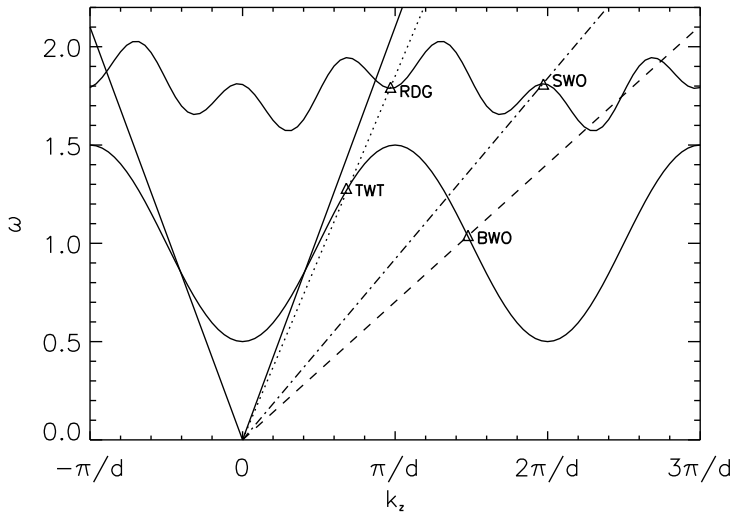

Figure 4.1: Interactions between the normal modes of a cavity with modulation period d and three different electron beams (indicated by the dotted, dashed, and dash-dotted lines). The triangles correspond to the four different radiation sources **BWO**, **TWT**, **RDG**, *and* **SWO**.

developed was a BWO in 1970 [63]. Continuous variation of the resonance frequency is possible within a frequency band by varying the electron beam velocity . In TWTs the interacting waves propagate in the same direction as the electron beam. The electrons have a typical energy of 0.5-0.9MeV and they constitute an electric current of normally around 1kA. To isolate the input signal from the output signal, and thereby avoid unwanted oscillations, it is common to have a two-step waveguide with a damping region in between. Efficiency can also be increased by using a "tapered" waveguide, that is, the phase speed is reduced as the electrons gradually loose their kinetic energy. This is achieved by modifying the walls of the tube in the output end of the tube. Efficiency of more than 45 % with an output power of around 400 MW has been achieved using this method [9]. Unfortunately, this power is typically distributed over a fairly wide frequency band with up to 50% of the power located in asymmetric side bands. Ongoing research in this field focuses on for example plasma-filled TWTs [65], utilizing radial hybrid modes [85] and bunch compression [64].

In BWOs, the microwaves are reflected in the far end of the tube, causing waves to propagate backwards relative to the electron motion. It is these reflected waves that interact resonantly with the electrons so that a growth in field strength can take place. BWOs used to be less efficient than TWTs, but the last few decades of research, for instance on "tapered" waveguides [50] and on including cyclotron resonant interactions [62], has contributed to reducing the difference between the two. Still, there are other Cerenkov devices available that surpass both BWOs and TWTs when it comes to output power. A **Relativistic Diffraction Generator (RDG)** can deliver gigawatts of power with a pulse length of around $0.7\mu s$ for wave lengths around 5mm [20], while a **Multiwave Cerenkov Generator (MWCG)** has been reported to produce 5-10GW for 80-100ns in the 3-cm

band by carefully tuning the magnetic field strength and the electron beam diameter [21].

4.1 Dispersion relation for linear waves in a sinusoidally-rippled waveguide

To illustrate the type of interactions one utilizes in O-type Cerenkov devices, we will derive the dispersion relation for linear TM_{0p}-mode waves in a Cerenkov device assuming an annular electron beam with radius r_b [72]. The waveguide is sylindrical with a radius r_w that varies along the axis of symmetry as

$$r_w(z) = r_0[1 + \kappa \sin(h_0 z)]. \tag{4.1}$$

Apart from the axial variation of r_w, this problem is identical to that solved in section 3.4.1. We will therefore in the following discussion refer to results obtain in section 3.4.1 whenever this is appropriate.

4.1.1 General solution for an annular electron beam

As done in section 3.4.1, we assume the presence of a strong, axial symmetric magnetic field that prevents any motion not parallel to the symmetry axis. Based on this assumption, we restrict ourselves to looking for a TM_{0p}-mode solution. Due to the periodic modulation of the waveguide, an expansion of all perturbed quantities δf associated with the electromagnetic waves is possible according to the **Floquet** theorem. Given the modulation period h_0 of the waveguide, δf can be written as

$$\delta f = \sum_{n=-\infty}^{\infty} \delta f_n(r) \exp[i(k_n z - \omega t)], \tag{4.2}$$

where $k_n = k_0 + nh_0$ and $-h_0/2 \leq k_0 < h_0/2$. Similarly, we define $\Gamma_n = (\omega/c)^2 - k_n^2$. Now, we want to solve the wave equation 2.7 for δE_{zn} in much the same way as was done for δE_z in section 3.4.1. The general form of δE_{zn} is given by equation 3.40. Requirements put on the solution due to the electron beam resulted in equations 3.43 and 3.50 relating the three parameters A_n, B_n, and C_n. As a consequence, $\delta E_z zn$ can now be written as

$$E_{zn} = A_n \begin{cases} J_0(\Gamma_n r) & 0 \leq r \leq r_b \\ J_0(\Gamma_n r) - \alpha \frac{\pi}{2} \left(\frac{\Gamma_n c}{\omega - k_n v_b} \right)^2 J_0(\Gamma_n r_b) \left[J_0(\Gamma_n r) Y_0(\Gamma_n r_b) - J_0(\Gamma_n r_b) Y_0(\Gamma_n r) \right] & r_b < r < r_w, \end{cases} \tag{4.3}$$

where α, as before, is defined by equation 3.52.

4.1.2 Restriction of the solution due to the outer boundary condition

We assume that the outer wall is perfectly conducting, implying that the tangential component of the $\boldsymbol{E}$ field relative to the wall should vanish at $r = r_w(z)$, where $r_w(z)$ is given by equation 4.1. A

tangential vector to the wall can be defined as $\boldsymbol{t} = (dr_w/dz)\hat{\boldsymbol{e}}_r + \hat{\boldsymbol{e}}_z$, where $\hat{\boldsymbol{e}}_r$ and $\hat{\boldsymbol{e}}_z$ are unit vectors in the r and z directions, respectively. The outer boundary condition can therefore be formulated as

$$\boldsymbol{t} \cdot \boldsymbol{E}\big|_{r=r_w} = 0. \tag{4.4}$$

If we insert the expression for $\boldsymbol{t}$ and use equation 3.41 to eliminate E_r, we get

$$e^{-i(k_0 z - \omega t)} \sum_{n=-\infty}^{\infty} \left(i \frac{k_n}{\Gamma_n^2} \frac{dE_{zn}}{dr} \frac{dr_w}{dz} + E_{zn} \right) e^{inh_0 z} \Big|_{r=r_w} = 0. \tag{4.5}$$

From using the chain rule we know that

$$\frac{dE_{zn}(r)}{dr}\Big|_{r=r_w(z)} \frac{dr_w}{dz} = \frac{dE_{zn}(z)}{dz}, \tag{4.6}$$

which makes it possible to rewrite the boundary condition, equation 4.4, as

$$\sum_{n=-\infty}^{\infty} A_n e^{inh_0 z} \left(1 + i \frac{k_n}{\Gamma_n^2} \frac{d}{dz} \right) \left\{ J_{nw} - \alpha \frac{\pi}{2} \left(\frac{\Gamma_n c}{\omega - k_n v_b} \right)^2 J_{nb} \left[J_{nw} Y_{nb} - J_{nb} Y_{nw} \right] \right\} = 0. \tag{4.7}$$

We have here introduced a simplified notation of Bessel functions, generally formulated as $\zeta_{nw} = \zeta_0(\Gamma_n r_w)$ og $\zeta_{nb} = \zeta_0(\Gamma_n r_b)$. The constant phase factor $\exp[i(k_0 z - \omega t)]$ has also been eliminated.

4.1.3 Fourier expansion of the solution

In order to obtain a solution independent of z, we will make a Fourier expansion of the solution. If we write equation 4.7 as

$$\sum_{n=-\infty}^{\infty} A_n f_n(\omega, k_n, z) = 0 \tag{4.8}$$

on a compact form, $f_n(\omega, k_n, z)$ can be expressed through a Fourier expansion as

$$f_n(\omega, k_n, z) = \sum_{m=-\infty}^{\infty} D_{mn}(\omega, k_n, k_m) e^{imh_0 z}, \tag{4.9}$$

where the Fourier coeffisients, in slightly simplified notation, is given by

$$D_{mn} = \frac{1}{z_0} \int_{-3z_0/4}^{z_0/4} e^{-imh_0 z} f_n(z) dz. \tag{4.10}$$

The integration limits, now written as z_a and z_c for short, can be freely choosen as long as the integration interval covers exactly one period of f_n. Replacing f_n in equation 4.10 with the expression in 4.9 and defining $p \equiv n - m = (k_n - k_m)/h_0$, result in

$$\begin{aligned} D_{mn} &= \frac{1}{z_0} \int_{z_a}^{z_c} e^{iph_0 z} \left(1 + i \frac{k_n}{\Gamma_n^2} \frac{d}{dz} \right) \left[J_{nw} - \alpha \left(\frac{\Gamma_n c}{\omega - k_n v_b} \right)^2 J_{nb} \left(J_{nw} Y_{nb} - J_{nb} Y_{nw} \right) \right] && (4.11) \\ &= K_{mn} - \alpha \left(\frac{\Gamma_n c}{\omega - k_n v_b} \right)^2 J_{nb} L_{mn}. && (4.12) \end{aligned}$$

Please notice that J_{nw} and Y_{nw} are functions of $\sin(h_0 z)$. Let us now take a closer look at the first term in the expression of D_{mn}, K_{mn}. Using partial integration, we get

$$K_{mn} = \frac{1}{z_0}\left\{\int_{z_a}^{z_c} e^{iph_0 z} J_{nw} dz + \frac{ik_n}{\Gamma_n^2}\left[e^{iph_0 z} J_{nw}\Big|_{z_a}^{z_c} + iph_0 \int_{z_a}^{z_c} e^{iph_0 z} J_{nw} dz\right]\right\} \quad (4.13)$$

$$= \frac{1}{z_0}\left[1 + \frac{(k_n - k_m)k_n}{\Gamma_n^2}\right]\int_{z_a}^{z_c} e^{iph_0 z} J_{nw} dz \quad (4.14)$$

$$= \frac{\omega^2 - k_m k_n c^2}{z_0 \Gamma_n^2 c^2}\int_{z_a}^{z_c} e^{iph_0 z} J_{nw} dz. \quad (4.15)$$

Since J_{nw} is a function of $\sin(h_0 z)$, it is desirable to express $e^{iph_0 z}$ as a function of $\sin(h_0 z)$ and $\cos(h_0 z)$. For specific values of p, $e^{ip\theta}$ can be expressed as

$$e^{ip\theta} = \begin{cases} 1, & p = 0 \\ \cos\theta \pm i\sin\theta, & p = \pm 1 \\ 1 - 2\sin^2\theta \pm i2\sin\theta\cos\theta, & p = \pm 2 \\ (1 - 4\sin^2\theta)\cos\theta \pm i\sin\theta(3 - 4\sin^2\theta), & p = \pm 3 \\ 1 - 8\sin^2\theta(1 - \sin^2\theta) \pm i2\sin\theta\cos\theta(1 - 2\sin^2\theta), & p = \pm 4 \end{cases} \quad (4.16)$$

and so forth. Since $\sin(h_0 z)$ is symmetric and $\cos(h_0 z)$ is anti-symmetric about $z_b = -z_0/4 \equiv (z_a + z_c)/2$, the integral of terms in equation 4.13 proportional to $\cos(h_0 z)$ will equal zero, the remaining part of the integral can be written as

$$K_{mn} = 2\frac{\omega^2 - k_m k_n c^2}{z_0 \Gamma_n^2 c^2}\int_{z_b}^{z_c} e^{iph_0 z} J_{nw}(\sin(h_0 z)) dz. \quad (4.17)$$

By performing the substitution $v = \sin(h_0 z)$, so that $\cos(h_0 z) = \sqrt{1 - v^2}$ in the interval from z_b to z_c, K_{mn} can finally be written as

$$K_{mn} = \frac{\omega^2 - k_m k_n c^2}{\pi \Gamma_n^2 c^2}\int_{-1}^{1} \frac{P_{mn}(v)}{\sqrt{1 - v^2}} J_{nw}(v) dv \quad (4.18)$$

where

$$P_{mn}(v) = \begin{cases} 1, & p = 0 \\ \pm iv, & p = \pm 1 \\ 1 - 2v^2, & p = \pm 2 \\ \pm iv(3 - 4v^2), & p = \pm 3 \\ 1 - 8v^2(1 - v^2), & p = \pm 4. \end{cases} \quad (4.19)$$

If we define

$$I_{mn}^{\zeta} = \frac{1}{\pi}\int_{-1}^{1} \frac{P_{mn}(v)}{\sqrt{1 - v^2}} \zeta_{nw}(v) dv, \quad (4.20)$$

where ζ_{nw} again represents one of the Bessel functions $J_0(\Gamma_n r_0(1 + \kappa v))$ or $Y_0(\Gamma_n r_0(1 + \kappa v))$, the total Fourier coefficient $D_{mn}(\omega, k_n, k_m)$ can be expressed as

$$D_{mn}(\omega, k_n, k_m) = \left(\frac{\omega^2 - k_m k_n c^2}{\Gamma_n^2 c^2}\right)\left[I_{mn}^J - \alpha\left(\frac{\Gamma_n c}{\omega - k_n v_b}\right)^2 J_{nb}\left(I_{mn}^J Y_{nb} - I_{mn}^Y J_{nb}\right)\right]. \quad (4.21)$$

The dispersion relation is finally obtained by solving the equation

$$\det[\boldsymbol{\mathcal{D}}] = 0, \tag{4.22}$$

where $\boldsymbol{\mathcal{D}}$ is a matrix with elements D_{mn}.

4.1.4 Specific solution of the dispersion relation

The size of the matrix $\boldsymbol{\mathcal{D}}$ can in most cases be restricted to 5×5 and the obtained solution would still be reasonably accurate [72]. If we first take a look at the case where no electron beam is present ($I_b = \alpha = 0$), $\omega r_0/c$ will in this case be a function of $k_0 r_0$, where ω is real. The model then only depends on the parameters κ og $h_0 r_0$. The top plot in figure 4.2 shows the solution of equation 4.22 for $\kappa = 0.077$ and $h_0 r_0 = 26\pi/11$ [72]. The vertical axis on the right hand side indicates the frequency measured in GHz for the case $r_0 = 1.3$cm. The 5 curves in the plot correspond to the 5 lowest TM-modes. If one introduces an electron beam with a current of $I_0 = 8$kA and a relativistic mass factor of $\gamma_0 = 1.91$ at the radius $r_b = 0.5$cm, the solution will become as shown in the bottom plot of figure 4.2. The dispersion curves that represent structure waves are found, with a few exceptions, close to the corresponding curves in the case with no beam present. In addition, two more curves are present, both starting at the origin, that represent space charge waves. Stable interactions (marked with a green circle) between the TM_{01} curve and the fastest of the space charge waves are found near $\omega r_0/c = 4$ and $k_0 r_0 = 4$. This causes the two waves to switch properties for larger values of k_0.

5 M-type devices

In M-type devices, electrons undergoing $\boldsymbol{E} \times \boldsymbol{B}$ drift interact with a wave field to produce microwave radiation. A necessary requirement is therefore that the drift velocity of the electrons, normal to both the $\boldsymbol{E}$ and $\boldsymbol{B}$ fields, are roughly equal to the phase speed of the electromagnetic waves. At the same time, the electrons emitted from the cathode should be prevented from reaching the anode, and thereby short-circuiting the system. We will start by studying these criteria more closely. Later, we will review briefly three specific devices, the well-established **relativistic magnetron**, the **crossed-field amplifier (CFA)**, and the more recently developed **Magnetically Insulated Transmission Line Oscillator (MILO)**.

5.1 Planar Brillouin flow

We will study the $\boldsymbol{E} \times \boldsymbol{B}$ drift of a relativistic electron beam in the region between an emitting cathode at zero electric potential and an anode at potential V. The distance between the cathode and the anode is d, as shown in figure 5.1. We assume space-charge-limited flow (see e.g. [40]), that is $E_x(x = 0) = 0$. This analysis has been presented by Davidson et al. [28].

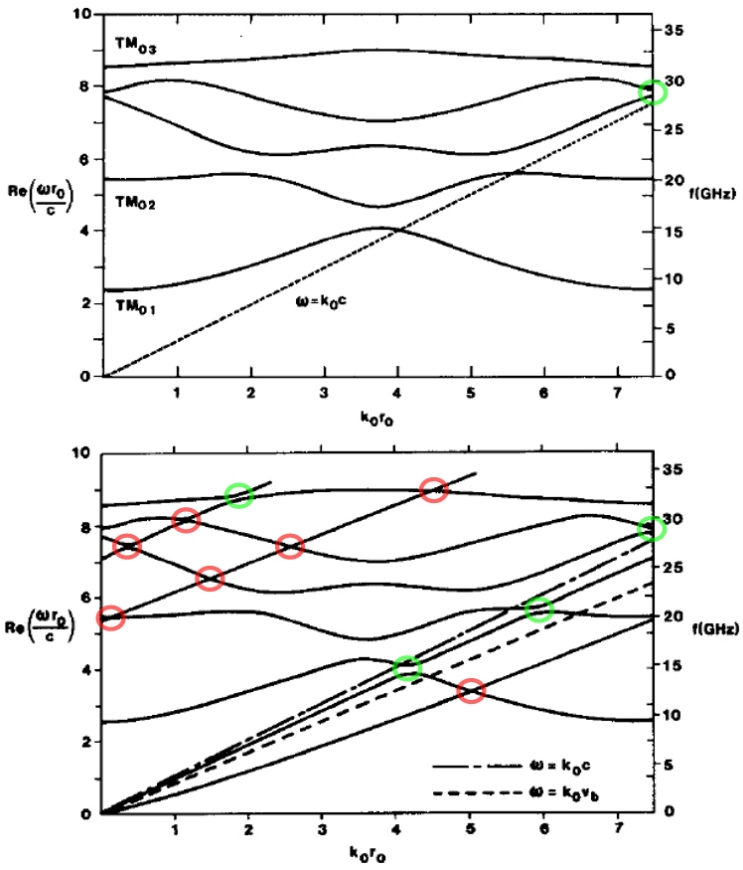

Figure 4.2: Solutions of 4.22 with $r_0 = 1.3$cm, $\kappa = 0.077$, $h_0 r_0 = 26\pi/11$, and $I_b = 0$ (top plot) and $I_0 = 8$kA (bottom plot). In the latter case, $\gamma_0 = 1.91$ and $r_b = 0.5$cm. The figure is, with some minor modifications, taken from [72].

5.1.1 Equilibrium properties

In general, an equilibrium solution is characterized by the fact that all time-dependent terms should vanish. In this case, we are left with purely a $\boldsymbol{E}_0 \times \boldsymbol{B}_0$ drift, where we assume the following model:

$$\boldsymbol{E}_0(\boldsymbol{r}) = E_x(x)\hat{\boldsymbol{e}}_x, \tag{5.1}$$

$$\boldsymbol{B}_0(\boldsymbol{r}) = B_z(x)\hat{\boldsymbol{e}}_z, \tag{5.2}$$

$$n_0(\boldsymbol{r}) = n_0(x), \tag{5.3}$$

$$\boldsymbol{v}_0(\boldsymbol{r}) = v_y(x)\hat{\boldsymbol{e}}_y. \tag{5.4}$$

Based on this model it can be concluded that the left hand side of the momentum equation 2.10, will be zero:

$$0 = -en_0(x)[E_x(x) + v_0(x)B_z(x)]. \tag{5.5}$$

If $n_0(x) > 0$, the drift velocity becomes

$$v_0 = -\frac{E_x(x)}{B_z(x)}. \tag{5.6}$$

This is the so-called $\boldsymbol{E} \times \boldsymbol{B}$ drift. By combining the expression for the drift with the Ampére-Maxwell's law (assuming $\partial \boldsymbol{E}/\partial t = 0$) , equation 2.2,

$$\frac{\partial B_z}{\partial x} = \mu_0 e n_0(x) v_0 = -\mu_0 e n_0(x)\frac{E_x(x)}{B_z(x)} \tag{5.7}$$

and Poisson's equation, equation 2.3,

$$\frac{\partial E_x}{\partial x} = -\frac{en_0(x)}{\epsilon_0}, \tag{5.8}$$

we get

$$\frac{\partial B_z^2(x)}{\partial x} = c^{-2}\frac{\partial E_x^2(x)}{\partial x}. \tag{5.9}$$

This means that $B_z^2(x) - c^{-2}E_x^2(x)$ is a constant quantity. Using equations 2.11 and 5.6, we also get that $\gamma_0(x) \propto B_z(x)$, where $\gamma_0(x) \equiv \gamma(v_0(x))$.

Relativistic Brillouin flow is characterized by the condition that the total energy of an electron fluid element is uniform across the electron layer. Since the total energy at $x = 0$ is equal to zero, the condition of energy conservation can be expressed as

$$[\gamma_0(x) - 1]m_e c^2 - e\phi_0(x) = 0. \tag{5.10}$$

Differentiating 5.10 and using the identity $E_x(x) = -\partial\phi_0/\partial x$ and equations 5.6 to 5.9, we obtain the following condition for relativistic Brilloiun flow:

$$\left(\frac{eB_z(x)}{\gamma_0(x)m_e}\right)^2 = \frac{e^2 n_0(x)}{\epsilon_0 \gamma_0(x) m_e} = \text{constant}. \tag{5.11}$$

This result can be rewritten as $\omega_c^2(x)/\gamma^2(x) = \omega_p^2(x)/\gamma(x)$, where the left and right hand sides are the relativistic cyclotron and plasma frequencies, respectively, at position x. Note also that

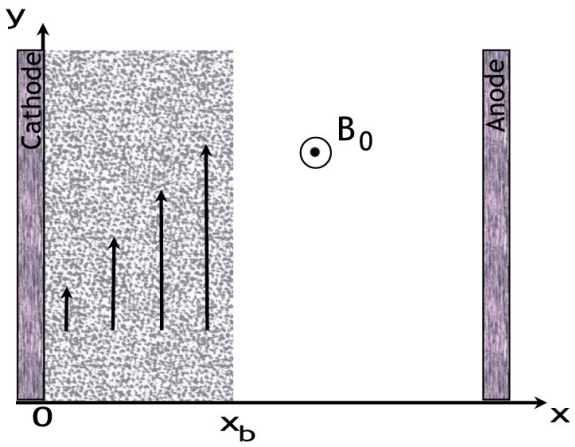

Figure 5.1: An electron layer extends from $x = 0$ to $x = x_b$. The magnetic field in the vacuum region, $x = x_b$ to $x = d$, is $B_0\hat{\boldsymbol{e}}_z$.

$B_z(x)$, $\gamma_0(x)$, and $n_0(x)$ all are proportional in the interval $0 \leq x < x_b$. To find e.g. $B_z(x)$, we can differentiate equation 5.7, use equation 5.8 to eliminate $\partial E_x/\partial x$, and utilize the fact that $n_0(x)/B_z(x)$ is a constant. We then find that

$$\frac{\partial^2 B_z(x)}{\partial x^2} - \kappa^2 B_z(x) = 0, \tag{5.12}$$

where

$$\kappa = e\mu_0 c \frac{n_0(x)}{B_z(x)} \tag{5.13}$$

is a constant. The solution to equation 5.12 is

$$B_z(x) = \begin{cases} B_0 \frac{\cosh(\kappa x)}{\cosh(\kappa x_b)} & 0 \leq x < x_b \\ B_0 & x_b < x \leq d, \end{cases} \tag{5.14}$$

where B_0 is the uniform magnetic field parallel to the symmetry axis in the interval $x_b < x \leq d$.

With γ_0 being proportional to B_z and $\gamma_0(0) = 1$, we find that $\gamma_0(x) = \cosh(\kappa x), 0 \leq x < x_b$. This result can be put into equation 5.10. In the interval $x_b \leq x < d$ we have $\partial^2\phi_0/\partial x^2 = 0$. We require ϕ_0 and $\partial\phi_0/\partial x$ to be continuous for the entire interval, leading to the following electric potential:

$$\frac{e\phi_0(x)}{m_e c^2} = \begin{cases} \cosh(\kappa x) - 1 & 0 \leq x < x_b \\ \cosh(\kappa x_b) - 1 + \kappa(x - x_b)\sinh(\kappa x_b) & x_b \leq x \leq d. \end{cases} \tag{5.15}$$

Normalized anode potential can now be coupled to the width of the Brillouin layer, x_b, through the expression

$$\frac{eV}{m_e c^2} = \cosh(\kappa x_b) - 1 + \kappa(d - x_b)\sinh(\kappa x_b). \tag{5.16}$$

It is also desirable to couple B_0 to the initial magnetic field strength B_f found between the anode and the cathode prior to the formation of the Brillouin layer. This can be done by taking into account the conservation of magnetic flux, that is

$$\int_0^d B_z(x)dx = \text{constant} \Longrightarrow B_f d = \frac{B_0}{\kappa}\tanh(\kappa x_b) + B_0(d - x_b). \tag{5.17}$$

Inserting $B_0 = B_z(0)\cosh(\kappa x_b)$ and utilizing the identity $eB_z(0) = \kappa m_e c$ (easily verified by combining equations 5.11 and 5.13), we can rewrite equation 5.17 as

$$\frac{eB_f d}{m_e c} = \sinh(\kappa x_b) + \kappa(d - x_b)\cosh(\kappa x_b). \tag{5.18}$$

If the Brillouin layer were to fill the entire interval between the anode and the cathode, that is $x_b = d$, the system would be short-circuited. By combining equations 5.16 and 5.18, we can find a relation, called the **Hull limit**, between the anode potential and the initial magnetic field strength for this special case. The potential in this case, known as the **Hull cutoff voltage** (V_H) is given as

$$\frac{eV_H}{m_e c^2} = \sqrt{1 + \left(\frac{eB_f d}{m_e c}\right)^2} - 1. \tag{5.19}$$

To achieve wave excitation in e.g. a relativistic magnetron, the anode potential must therefore be $V < V_H(B_f)$. Another condition that should be fulfilled in order to achieve efficient interaction between the wave field and the electrons, is the requirement of resonance. That is, the fastest electrons in the Brillouin layer (found at $x = x_b$) should have a velocity at least equal to the phase speed of the exited waves, $v_p = \omega/k_y \equiv \beta_p c$. This implies that the anode potential much be larger than the so-called **Bunemann-Hartree threshold**. If we combine equations 5.16 and 5.18 in such a way that $\kappa(d - x_b)$ is eliminated, we get

$$\frac{eV}{m_e c^2} = \frac{eB_f d}{m_e c}\tanh(\kappa x_b) - 1 + \frac{1}{\cosh(\kappa x_b)}. \tag{5.20}$$

Since $\gamma_0(x) = \cosh(\kappa x_b)$, we can easily verify that $v_0(x) = c\tanh(\kappa x_b)$. If we in addition require that $v_0(x) = \beta_p c$ at the threshold voltage V_{BH}, we get the expression

$$\frac{eV_{BH}}{m_e c^2} = \frac{eB_f d}{m_e c}\beta_p - 1 - \sqrt{1 - \beta_p^2}. \tag{5.21}$$

The Hull limit and the Bunemann-Hartree threshold is plotted in a B_f-V diagram in figure 5.2.

5.1.2 Extraordinary-mode eigenvalue equation

Starting with the equilibrium solution just described, we will study properties of so-called extraordinary-mode, linear waves. This is electromagnetic waves where the perturbed electric field is always normal to the magnetic field. Following the approach described in appendix A, we assume the perturbations are of the form

$$\delta f(x, y, t) = \sum_{k=-\infty}^{\infty} \delta f(x, k)e^{i(ky - \omega t)}, \tag{5.22}$$

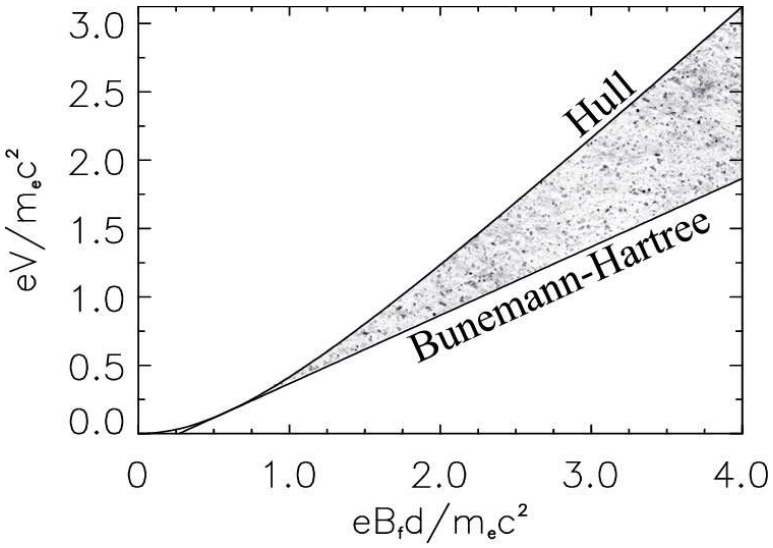

Figure 5.2: **Bunemann-Hartree threshold** *and* **Hull limit** *delimits the normalized parameter space of voltage (eV/m_ec^2) and initial magnetic field strength (eB_fd/m_ec^2) that can produce an effective and stable interaction between the electrons in the Brillouin layer and the wave field. In this case with $\beta_p = 0.5$.*

where the amplitudes δn, δv_x, δv_y, $\delta\gamma$, δE_x, δE_y and δB_z are assumed to be small enough for a linear approximation to be valid. Bearing in mind that the $\boldsymbol{E} \times \boldsymbol{B}$ drift found in the equilibrium solution is in the y-direction, γ will in the linear approximation depend on V_y only. By differentiating γ with respect to v_y, a linear approximation to $\delta\gamma$ is found to be

$$\delta\gamma = \gamma_0^3 \frac{v_0}{c^2} \delta v_y. \tag{5.23}$$

As a consequence, we get

$$\frac{\partial}{\partial u}(\gamma_0 \delta v_y + v_0 \delta\gamma) = \gamma_0^3 \frac{\partial \delta v_y}{\partial u}, \tag{5.24}$$

where u could be equivalent to either t or y. Correspondingly, we have

$$\frac{\partial}{\partial x}(\gamma_0 v_0) = \gamma_0^3 \frac{\partial v_0}{\partial x}. \tag{5.25}$$

Linearizing the continuity equation, equation 2.9, gives us

$$\frac{\partial \delta n}{\partial t} + \frac{\partial}{\partial y}(v_0 \delta n + n_0 \delta v_y) + \frac{\partial}{\partial x}(n_0 \delta v_x) = 0, \tag{5.26}$$

which assuming perturbations of the form 5.22 becomes

$$-i(\omega - k v_0)\delta n = -ik n_0 \delta v_y - \frac{\partial}{\partial x}(n_0 \delta v_x). \tag{5.27}$$

The x-component of the momentum equation, equation 2.10, on linearized form gives us

$$\gamma_0 \frac{\partial \delta v_x}{\partial t} + v_0 \frac{\partial}{\partial y}(\gamma_0 \delta v_x) = -\frac{e}{m}(\delta E_x + v_0 \delta B_z + B_z \delta v_y) \tag{5.28}$$

which becomes

$$-i(\omega - kv_0)\delta v_x + \frac{\omega_c}{\gamma_0}\delta v_y = -\frac{e}{\gamma_0 m}(\delta E_x + v_0 \delta B_z). \tag{5.29}$$

The corresponding y-component is

$$\frac{\partial}{\partial t}(\gamma_0 \delta v_y + v_0 \delta\gamma) + \delta v_x \frac{\partial}{\partial x}(\gamma_0 v_0) + v_0 \frac{\partial}{\partial y}(\gamma_0 \delta v_y + v_0 \delta\gamma) = -\frac{e}{m}(\delta E_y - B_z \delta v_x). \tag{5.30}$$

We eliminate $\delta\gamma$ by utilizing relations 5.23 and 5.24. To rewrite $\partial(\gamma_0 v_0)/\partial x$ we first use the result from equation 5.25 to eliminate the derivative of γ_0. Then, we insert the expression for v_0 from equation 5.6 and use equations 5.7 and 5.8 to express $\partial(v_0)/\partial x$ as $\gamma_0^2\omega_p^2/\omega_c$. In short, the y-component of the momentum equation can now be written as

$$-i(\omega - kv_0)\gamma_0^2 \delta v_y + \frac{\gamma_0\omega_p^2 - \omega_c^2}{\gamma_0\omega_c}\delta v_x = -\frac{e}{\gamma_0 m}\delta E_y. \tag{5.31}$$

In addition, we will need the linearized versions of Faraday's law,

$$i\omega\delta B_z = \frac{\partial \delta E_y}{\partial x} - ik\delta E_x, \tag{5.32}$$

Ampére-Maxwell's law (x-component only),

$$ik\delta B_z = -e\mu_0 n_0 \delta v_x - i\frac{\omega}{c^2}\delta E_x, \tag{5.33}$$

and Poisson's law,

$$\frac{\partial \delta E_x}{\partial x} + ik\delta E_y = -\frac{e}{\epsilon_0}\delta n. \tag{5.34}$$

We will also introduce the effective potential $\Phi_k(x)$, defined by

$$\Phi_k(x) = \frac{i}{k}\delta E_y(x, k,) \tag{5.35}$$

and the effective wave mass factor γ_w, defined by

$$\gamma_w = \frac{1}{\sqrt{1 - \omega^2/(k^2c^2)}}. \tag{5.36}$$

From equations 5.32 and 5.33 we find that δE_x and δB_z can be expressed as

$$\delta E_x = -\gamma_w^2 \left(\frac{\partial \Phi_k}{\partial x} + \frac{i\omega}{k^2c^2}\frac{en_0}{\epsilon_0}\delta v_x \right) \tag{5.37}$$

and

$$\delta B_z = \gamma_w^2 \left(\frac{\omega}{c^2 k}\frac{\partial \Phi_k}{\partial x} + \frac{i}{kc^2}\frac{en_0}{\epsilon_0}\delta v_x \right), \tag{5.38}$$

respectively. Substituting equations 5.27 and 5.37 into equation 5.34 gives us the following relation between Φ_k and the velocity perturbations:

$$\left[\frac{\partial^2}{\partial x^2} - \frac{k^2}{\gamma_w^2} \right] \Phi_k = -\frac{ie}{\epsilon_0\omega_b} \left\{ \alpha \frac{\partial}{\partial x}(n_0 \delta v_x) + \frac{ik}{\gamma_w^2}(n_0 \delta v_y) \right\} \tag{5.39}$$

where $\omega_b = \omega - kv_0$ and $\alpha = 1 - v_0\omega/c^2k$. Using equations 5.29 and 5.31 we can eliminate δv_x and δv_y from equation 5.39. After some algebra, the following eigenvalue equation for Φ_k is obtained:

$$\frac{\partial}{\partial x}\left\{[1+\chi_\perp]\frac{\partial \Phi_k}{\partial x}\right\} - k^2[1+\chi_\parallel]\Phi_k = \frac{k\alpha\Phi_k}{\omega_b}\frac{\partial}{\partial x}\left(\frac{\omega_p^2\omega_c}{\gamma_0^2\nu^2}\right), \tag{5.40}$$

where

$$\chi_\perp = \gamma_0\left(\frac{\alpha\omega_p\gamma_w}{\nu}\right)^2, \tag{5.41}$$

$$\chi_\parallel = \gamma_w^{-2} - 1 - \frac{\omega_p^2}{\gamma_0\nu^2}\left(\gamma_w^{-2} + \frac{\omega_p^2}{\gamma_0 c^2k^2}\right), \tag{5.42}$$

and

$$\nu^2 = \gamma_0^2\omega_b^2\left(1 + \frac{\omega_p^2\gamma_w^2}{c^2k^2}\right) + \frac{\gamma_0\omega_p^2 - \omega_c^2}{\gamma_0^2}. \tag{5.43}$$

If the equilbrium state is identical to the Brillouin flow, the equilibrium magnetic field will be given by equation 5.14. Since both γ_0 and n_0 should be proportional to the magnetic field strength in the interval $0 \leq x < x_b$, we can now solve the eigenvalue equation, equation 5.40, numerically to investigate the so-called **magnetron instability**. Figure 5.3 is taken from [28] and shows the solution for various choices of the normalized layer width, x_b/d, the self-field parameter, $S_e = \omega_p^2\gamma_0(x_b)/\omega_c^2$, and the normalized wave number, $ck/\hat{\omega}_{ce}$, where $\hat{\omega}_{ce} = \omega_c(x_b)/\gamma_0(x_b)$.

5.2 Relativistic magnetron

The conventional **magnetron** is widely used as the radiation source in a number applications such as in microwave ovens, in portable radar systems (X-/C-/S-band), and for plasma heating. Reasons for this is the high efficiency (typically 50-90%), compact size, reliability, and inexpensive manufacturing costs. A typical configuration is shown in figure 5.4 taken from a simulation using the commercially available **Particle-In-Cell (PIC)** code **MAGIC** [41]. In the relativstic case, electrons are emitted from the cathode (inner cylinder) through explosive emission. Due to the $\boldsymbol{E}$ field, the electrons are at first accelerated radially outwards. Then they are subjected to $\boldsymbol{E} \times \boldsymbol{B}$ drift that, assuming the relative strength of $\boldsymbol{E}$ and $\boldsymbol{B}$ lie within the **Hull limit**, prevents the electrons from reaching the anode. The electrons, through this process known as "magnetic shielding", form a cylindrical cloud, the aforementioned **Brillouin layer** . The small, resonant cavities on the inside of the anode modulate the electromagnetic field, and thereby determine the operating frequency of the magnetron. The magnetron in figure 5.4 is a π-mode configuration. Relativistic magnetrons operate with efficiency levels of 20-40% and output power levels around 5GW at frequency in the range of 1 to 8GHz. Pulse lengths are usually restricted to about 100ns, and the current should exceed 10kA. By replacing a permanent magnet with a current-driven magnetic field one can in principle achieve a time-varying magnetic field strength. The problem then is to also adjust the electric field accordingly to ensure the operation criteria is still met.

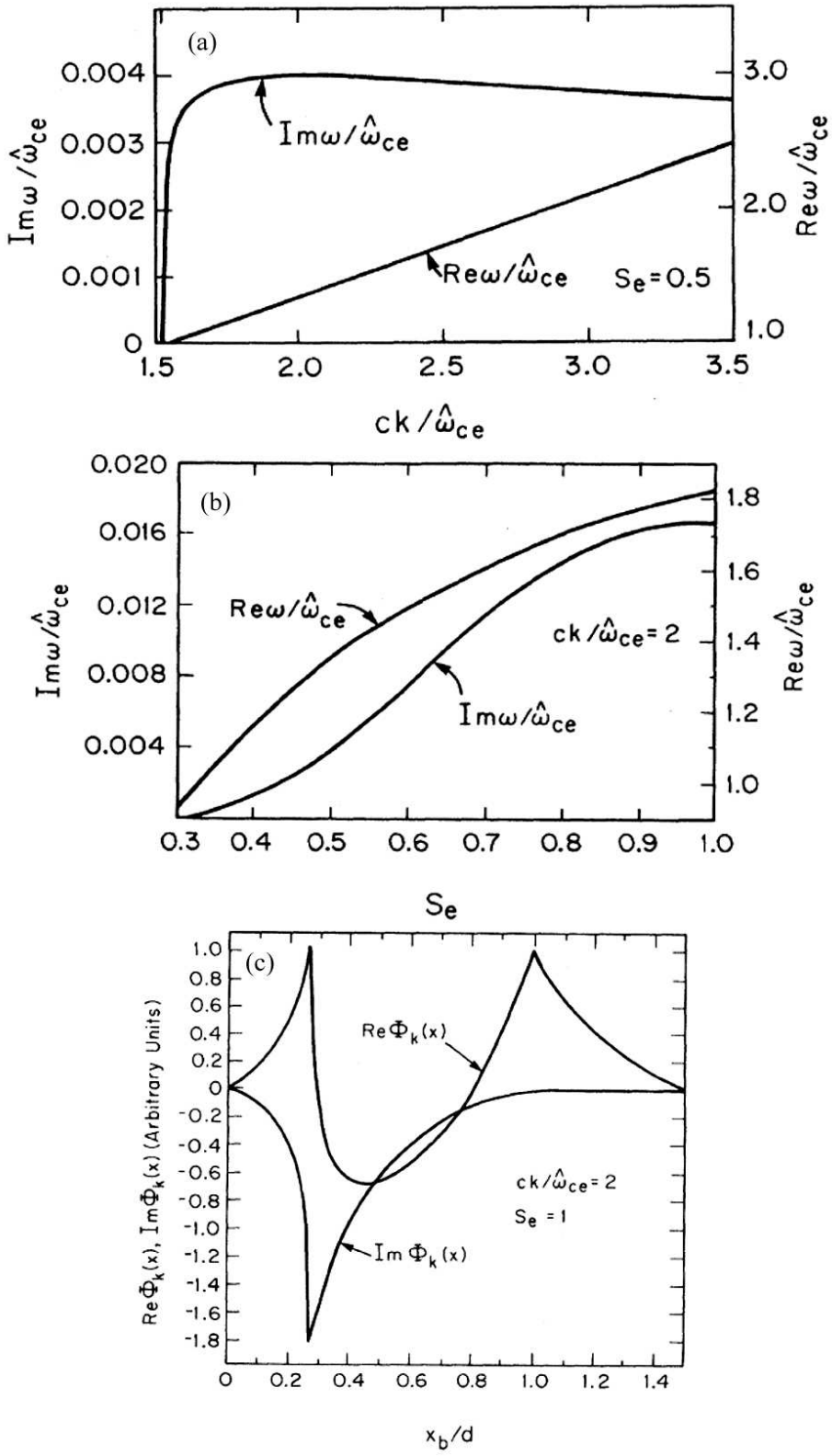

Figure 5.3: Linear growth properties of the magnetron instability: (a) Normalized growth rate (Im$\omega/\hat{\omega}_{ce}$) and real oscillation frequency (Re$\omega/\hat{\omega}_{ce}$) plotted as functions of $ck/\hat{\omega}_{ce}$ for $S_e = 0.5$ and $x_b/d = 2/3$. (b) Im$\omega/\hat{\omega}_{ce}$) and Re$\omega/\hat{\omega}_{ce}$ plotted as functions of S_e for $x_b/d = 2/3$ and $ck/\hat{\omega}_{ce} = 2$. (c) Imaginary and real effective potential plotted in normalized units as functions of x_b/d for $S_e = 1$ and $ck/\hat{\omega}_{ce} = 2$.

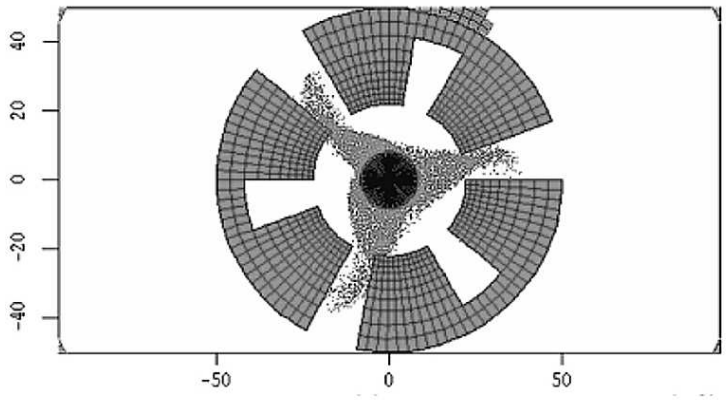

Figure 5.4: Simulation of a cylindrical magnetron [41] using the numerical code **MAGIC** *[42]. The inner cylinder functions as the cathode. The magnetic field ($\boldsymbol{B}$) is directed out of the plane. The snapshot is taken 30ns after externally applying a voltage of 260 kV. The spatial unit is millimetre.*

5.3 Crossed-field amplifiers (CFA)

Planar versions of the magnetron, known as **crossed-field amplifiers (CFA)**, also exist. A sketch of a π-mode CFA is shown in figure 5.5. The electron cloud is indicated in the sketch by the brown, semi-transparent layer. The thin field lines indicate the direction of the total electric field, while the thick, dotted arrows indicate the electron velocity field. We will refer to this sketch in the following discussion of the operation of both magnetrons and CFAs. The electrons enter the green-coloured region from the lower right corner due to the equilibrium drift caused by $\boldsymbol{E}_0$ and $\boldsymbol{B}_0$. The modification to the electric field in the green region then causes the drifting motion to turn towards the anode. The electrons there move closer to the anode and slows down in the horizontal drift. As a consequence, a so-called “spoke” is formed where the electron density increases in the anode cavity (the region between two consecutive vanes). Since the electrons are essentially moving parallel to the electric field, the electrons loose kinetic energy to the RF field. Since the electrons move closer to the anode, the electrons also loose potential energy to the RF field. In fact, the total energy loss in this region is dominated by the loss in potential energy.

Assuming the electrons cannot penetrate the anode surface, the density will build-up on the right-hand side of the vane marked ’-’. Eventually, the local field is sufficiently modified that electrons are pushed back towards the cathode. The equilibrium drift brings the electrons into the yellow region where the RF field has changed sign relative to what was the case in the green region. The drift motion is therefore turned towards the cathode, causing the electrons to move even closer to the cathode and therefore gains potential energy. The electrons, now moving essentially anti-parallel to the electric field, are accelerated and gains kinetic energy as well. The gain in total energy is at the expense of the RF field. However, the density in the yellow region will be lower then the

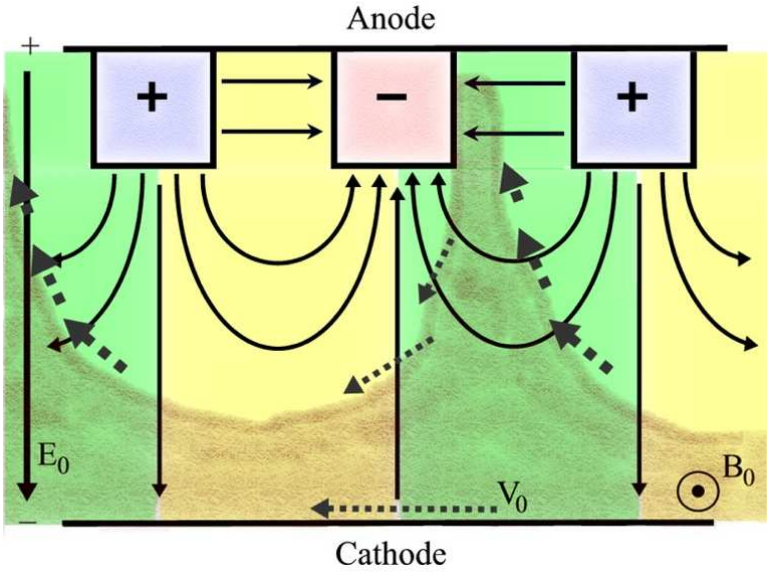

Figure 5.5: Sketch of a π-mode **crossed-field amplifier (CFA)** *illustrating the typical electron distribution (brown, semi-transparent layer) and velocities (thick, dotted arrows) together with the electric field (thin lines). The green and yellow colouring identifies regions of energy transfer to and from the RF field, respectively.*

corresponding density in the green region. As a consequence, a net transfer of energy *from* the electrons *to* the RF field is achieved as the electrons pass through the same number of green and yellow regions.

5.4 MILO

In devices of the type called **Magnetically Insulated Transmission Line Oscillator (MILO)** the magnetic field is generated by the current running through the cathode itself. These devices are in other words "self-isolating". This secures that the variations in $\boldsymbol{E}$ and $\boldsymbol{B}$ are in phase. A MILO device can have either a cylindrical or a plane geometry. An example of the former case is shown in figure 5.6 [43]. The cathode constitutes the lower boundary, while the anode serves as the upper boundary. The vanes are relatively thin disc-like modulations of the anode. A problem has been to achieve efficient radiation extraction as the electrons gradually loose energy and thereby fall out of synchronism with the dominant wave mode. This problem has to some extent been solved by reducing the length of the vanes as one gets nearer to the output region. To avoid reflected waves to propagate backwards, it is common to include a few extra long vanes, known as a Bragg reflector, at the far end of the interaction cavity. Recent results indicate efficiency levels of around 10% with about 2GW in the 1-2GHz frequency range [31, 32, 48]. The MILO is otherwise characterized by delivering high energy per mass per pulse. A compact MILO model, including a Marx generator and delivering about 1GW, has in recent years been developed in France where the approximate

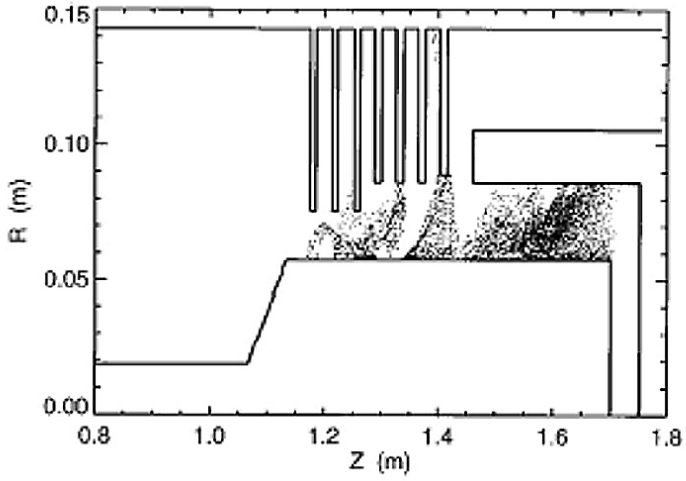

Figure 5.6: Simulation of a cylindrical **MILO** *constructed at* **Air Force Research Laboratory**. *The simulation is done with the code* **TWOQUICK** *in two (spatial) dimensions [43].*

length and diameter is 100cm and 20cm [26], respectively. On the other hand, the device is also regarded being less tunable than many other HPM devices as the frequency cannot be shifted by simply changing the voltage.

6 Virtual cathode oscillator (VCO)

The first microwave device based on the **virtual cathode** principle was developed in 1977 [58]. Devices of this type are usually very compact and distinguish themselves from other devices by requiring a current density that exceeds the space charge limit. This means that the energy associated with the electric potential exceeds the kinetic energy in the electron beam. The main mechanism behind the VCO, also referred to as the **Vircator**, is illustrated in figure 6.1. If the anode is shaped as a grid so that the electrons can pass through it, a cloud of electrons known as a virtual cathode can be formed behind the anode. Gradually, the electrostatic potential is reduced. The position and potential of the virtual cathode will oscillate. This oscillation will also modulate the density in the electron population that passes virtual cathode. There are therefore two different ways the microwave radiation can be generated, the *reflexing mechanism* that creates bunching of electrons inside the potential well between the cathode and the anode, and the *oscillating mechanism* that creates bunching of electrons due to the oscillatory behaviour of the virtual cathode. In any case, the frequency of the waves will equal the plasma frequency, which can be changed by simply changing the electron density. Relatively long pulse durations, up to $1\mu s$, can be achieved, but the reported efficiency for traditional configurations, up to 2-3%, has been too low. Not surprising, the radiation spectrum typically exhibits several distinct peaks.

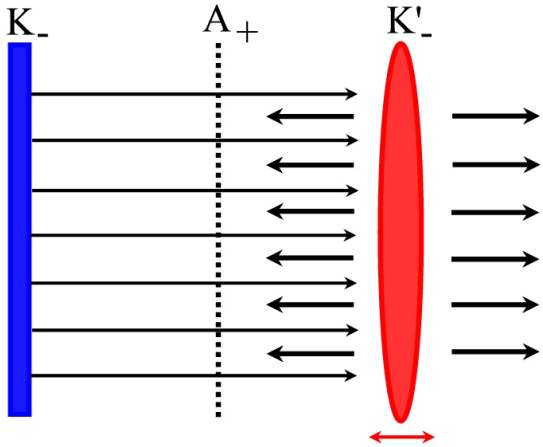

Figure 6.1: Illustration of the virtual cathode principle. The real cathode is marked K_-, the anode is marked A_+ and the virtual cathode is marked K'_- [53].

Several different devices have been constructed that utilize the principle of the VCO but which attempt to increase the efficiency. In the **Reflex Triode**, the anode is a high-voltage electrode, while the cathode is grounded. Efficiencies of about 10% has been reported with this device [47]. In the **Reditron**, the electrons are prevented from being reflected back into the anode-cathode (A-C) gap. This is achieved by having an externally applied axial magnetic field which guides the electrons through a small opening in the anode. On the other side of the anode the magnetic field strength is strongly reduced. Electrons reflected off the virtual cathode can therefore freely expand in the radial direction. The expansion prevent the electrons from re-entering the A-C gap. Experiments have so far shown roughly a doubling of the efficiency compared to ordinary VCO devices [27].

6.1 Steady-state VCO theory

In the following section we will consider a simple, one-dimensional model that illustrate some of the mechanisms behind the formation of a virtual cathode. It is a steady-state model taken from [46]. The electrons enter at the injection point where the electric potential ϕ equals zero. At the position of the virtual cathode, $\phi = -V_0$, $E = 0$, and a certain fraction of the electron beam is reflected back towards the injection point. Given that the electrons have no kinetic energy at the position of the virtual cathode, we can relate the relativistic mass factor, γ, to the electrostatic potential, ϕ, by applying the principle of energy conservation:

$$\gamma = 1 + \frac{e(V_0 + \phi)}{mc^2}. \tag{6.1}$$

The sum of the absolute values of the injected and reflected currents, J, can be expressed as

$$J = env = enc\sqrt{1 - \gamma^{-2}}. \tag{6.2}$$

From Poisson's equation, equation 2.3, and the expression for the electrostatic potential, equation 2.6 with $\boldsymbol{A} = 0$, we get

$$dE = -\frac{ne}{\epsilon_0}dx = \frac{ne}{\epsilon_0 E}d\phi. \tag{6.3}$$

We can replace the spatially varying n with the uniform J, and $d\phi$ with $d\gamma$ through the use of equations 6.2 and 6.1, respectively:

$$\frac{1}{2}d(E^2) = \frac{Jmc}{e\epsilon_0}d(\sqrt{\gamma^2 - 1}). \tag{6.4}$$

Equation 6.4 is on an easily integratable form which, when we take into account that $E = 0$ and $\gamma = 1$ at the position of the virtual cathode, give us a relation between E and γ, or between E and ϕ. The electric field profile between the injection point and the virtual cathode becomes

$$E = \left(\frac{2Jmc}{e\epsilon_0}\right)^{1/2}\left(\gamma^2 - 1\right)^{1/4} = \left(\frac{2Jmc}{e\epsilon_0}\right)^{1/2}\left[\left(1 + \frac{e(V_0 + \phi)}{mc^2}\right)^2 - 1\right]^{1/4}. \tag{6.5}$$

The time $\bar{\tau}$ it takes a reflected electron to return from the virtual cathode at $x = x_V$, to the injection point at $x = 0$ is of interest in the following discussion, and is found as

$$\bar{\tau} = \int_0^{\bar{\tau}} dt = -\int_{x_V}^0 \frac{dx}{v} = -\int_{x_V}^0 \frac{en}{J}dx = \int_0^{E(0)} \frac{\epsilon_0}{J}dE = \frac{\epsilon_0 E(0)}{J}. \tag{6.6}$$

If we use equations 6.2 and 6.5, we can replace J and $E(0)$, respectively, with expressions proportional to $\gamma_0 = \gamma(x = 0)$ and $n_0 = n(x = 0)$. In doing so, we can rewrite $\bar{\tau}$ as

$$\bar{\tau} = \sqrt{\frac{2\epsilon_0 m\gamma_0}{n_0 e^2}} = \sqrt{2\gamma_0}\omega_p^{-1}, \tag{6.7}$$

where ω_p is the non-relativistic plasma frequency.

7 Gyrotron

Gyrotrons, also known as **electron cyclotron masers (ECMs)**, are fast wave devices that first came into existence in the late 1950s, e.g. in [74]. The idea behind this development is to extract kinetic energy related to the gyrating motion of electrons in a magnetic field. Unlike most other known HPM sources, gyrotrons can produce highly efficient microwave generation in the (sub-)millimetre, as well as in the centimeter wave length range (illustrated i figur 7.1). Efficiency levels of 30-50% is common. A gyrotron will typically include the following components: An electron beam with a sufficiently large velocity component, $v_\perp$, normal to the beam and as indicated by the parameter $\alpha = v_\perp/v_{||}$, a smooth wave guide, and a magnetic field parallel to the electron beam.

The main mechanism for a resonant interaction between the electrons and the wave field is through a relativistic effect coupled to the gyro-motion. The cyclotron frequency in the relativistic case is

$$\omega_c = \frac{eB}{m_0\gamma} = \frac{eB}{m_0}\sqrt{1 - v^2/c^2}, \tag{7.1}$$

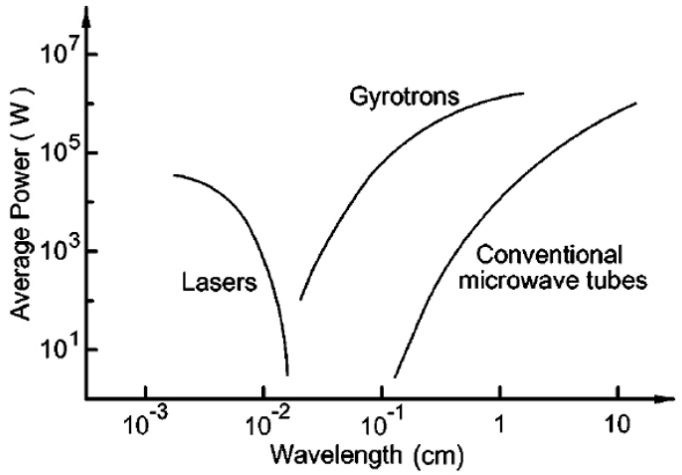

Figure 7.1: Comparison of average power for lasers, gyrotrons (ECMs), and other microwave sources. The gyrotrons are the only alternative with gigawatts output in the (sub-)millimeter parameter wave length range. [24]

and the Larmor radius is as always

$$r_L = \frac{v_\perp}{\omega_c}. \tag{7.2}$$

Looking at the example sketched in figure 7.2, we notice that the particles marked 1, 2, and 8 will have their rotational speed, $v_\perp$, reduced due to the electric field. From equations 7.1 and 7.2 we see that the cyclotron frequency increases and the Larmor radius decreases for these particles. This causes the electrons to move closer together and closer to the rotational centre. Equivalently, the particles marked 4, 5, and 6 will have their rotational speed increased, thereby reducing the cyclotron frequency and increasing the Larmor radius. These particles therefore move further apart and further away from the rotational centre. If the $\boldsymbol{E}$ field is circularly polarized with a frequency slightly higher than the cyclotron frequency, particles 1, 2, and 8 will have a greater net loss of kinetic energy than the corresponding kinetic energy gained by particles 4, 5, and 6. The wave field will in other words have gained energy in the process. This is the main mechanism behind gyrotron devices. By taking advantage of the interaction between gyrating electrons and a wave field with a frequency close to the cyclotron frequency, a class of devices has been developed that corresponds to the non-gyrating O-type devices (gyrotron, gyro-TWT, gyro-BWO, gyro-klystron).

Efficient operation of fast-wave gyrotrons requires the electrons initially to have a non-zero velocity component normal to the magnetic field. To produce a rotating electron beam is technically challenging if one at the same time requires a great degree of uniformity. The usual techniques often lead to a destructive spreading of momentum along the axis of rotation. There has therefore been a certain interest in developing gyrotron devices that can utilize electron beams without rotation. This is known as **slow-wave gyrotron** sources which make use of Cerenkov radiation. If the electrons initially have a velocity slightly larger than the phase speed of the waves, the interaction will lead to a clumping of electrons in the direction parallel to the magnetic field. This in turn causes energy to

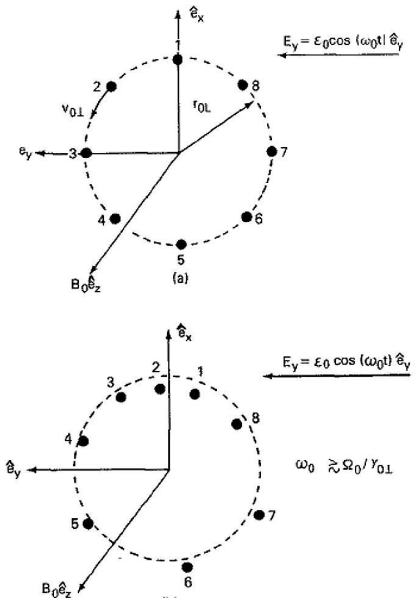

Figure 7.2: Main principles behind the **gyrotrons** *explained through illustration taken from [76]. Test particles in a gyrating motion are initially uniformly distributed (a). After several periods, the clumping of electrons is visible (b).*

be transferred from the beam to the wave field. To achieve electromagnetic waves with phase speed less than the speed of light (in vacuum), it is common to use wave guides filled with a dielectric material (plasma).

8 Free electron laser (FEL)

A **free electron laser (FEL)** can, unlike the other HPM sources described here, produce radiation that extends beyond the microwave regime, into both UV and visible. This is possible by letting electrons pass through a static magnetic field with spatially alternating polarization. This kind of structure is known as an **undulator** or a **wiggler**. The radiation is generated by fast-wave interactions where the electrons resonate with the electromagnetic field and the undulator. The wave length λ_s of the coherent radiation depends mainly on the electron energy as well as the period λ_u and amplitude B_u of the magnetic field produced by the undulator:

$$\lambda_s \approx \frac{\lambda_u}{2\gamma^2}\left[1 + \frac{(eB_u\lambda_u)^2}{2(2\pi mc)^2}\right], \tag{8.1}$$

[67]. As the electrons loose their energy to the wave field, the resonant coupling will be gradually be weakened. As is the case with other HPM sources, one can increase the efficiency by varying the undulator parameters in space so that it better fits the spatial variation of the electron energy. In the case of FEL, this can for instance be achieved by either reducing the period λ_u or the amplitude B_u

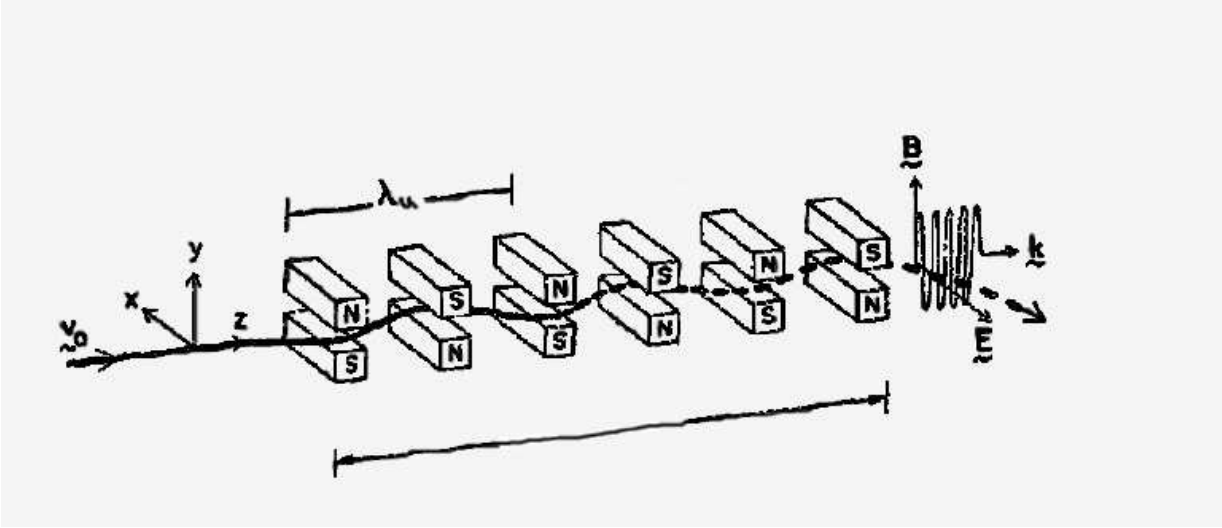

Figure 8.1: Basic sketch of the FEL structure (taken from [70]).

towards the far end of the undulator structure. This type of modification has been documented to result in a radiation efficiency of 20-30% [67, 77]. Similar techniques to increase the radiation power even more have been studied [70]. Sprangle, Tang & Manheimer [77] saw an order of magnitude increase in the power, while Orzechowski et al. reported in 1986 an almost 7 times increase in power (equivalent to 34% efficiency) for radiation at wavelength $\lambda_s \sim 1$cm. This was achieved by reducing B_u by roughly 50% towards the far end of the undulator structure [67].

9 Remaining research challenges

Great advances have been achieved over the last few decades in developing HPM devices that could have a potential as an electromagnetic weapon. Still, there are remaining issues in increasing output power and total radiated energy, while reducing the required mass and volume of the devices. As an example, the Vircator, one of the most compact and therefore most interesting HPM devices, can only deliver microwave radiation with an efficiency (the power ratio of high frequency output to low frequency input) of less than 10%. This means that the study of HPM sources, like the Vircator, is very important in realizing the idea of HPM weapons.

A key issue in this work is **pulse shortening**. Over the past 20 years or so, maximum output power of HPM devices has steadily increased. However, the increase in output power has also caused the typical pulse length to be decreased. As a consequence, the total radiated energy per pulse has stagnated at around 200-1000J [9]. Pulse shortening can be measured as the ratio between the pulse length of the microwave radiation and the pulse length of the electron beam. The phenomenon of pulse shortening usually occurs at field levels of more than 100kV/cm and at frequencies of around 1GHz. Physical causes to pulse shortening can be divided into 5 categories:

- **Suboptimal tube design:** Microwave tubes should be designed so that instabilities are avoided. This is achieved by keeping magnetic field strengths moderate (< 1T), and avoiding strong $\boldsymbol{E}$-field strengths near surfaces.

- **Spontaneous plasma generation:** This can occur near both the cathode and the anode, due to unwanted beam expansion or as a consequence of the beam hitting a surface. A result of plasma spontaneously being generated is that the diode impedance or the dominant wave modes might change and thereby weaken the coupling between the beam and the wave field.

- **Spontaneous electron currents:** Electrons emitted at the cathode can in some cases move opposite to the usual current direction, towards the pulse forming line, and thereby influence the diode impedance.

- **Field breakdown due to high $\boldsymbol{E}$-field strengths:** The phenomena of field breakdown is linked to the localized release of absorbed gases, and as such, is highly sensitive to surface treatment in cavity structures, to vacuum conditions, and to any plastic components in the vacuum envelope. Breakdown can also occur on the output window due to surface flashover.

- **Beam disruption:** Instabilities can destroy the specified geometry of the electron beam, which typically will affect the wave generation. A common instability creates magnetic filaments which causes the beam to break up into individual beamlets that can interact magnetically. This can occur if a background plasma exists.

The issue of pulse shortening has lead to a shift in research from increasing radiation power to increasing total radiation energy per pulse. Pulse shortening is thereby a keyword for the common challenges faced by HPM research today. Serving as a summary of the project **High-Power Microwave (HPM) MURI** it was in 2001 formulated 12 important research topics in the future development of HPM sources, ordered according to their viewed importance [9]. Here we briefly present 10 of these topics:

1. **Conditioning of HPM devices:** It is important to develop improved techniques for achieving vacuum and for avoiding contamination through gas emission from the tube walls. Relevant research needs to study in greater detail what effect conditioning has on the resulting power. Conditioning will typically have to depend on parameters such as e. g. repetition rates, tube type, materials, vacuum quality and field strengths. It will also be important to develop techniques for cost effective and industrialized techniques for large-scale conditioning of HPM devices.

2. **Development of new cathode technology:** Military HPM devices typically use so-called EEE (Explosive Electron Emission) cathodes in order to generate the high currents necessary to achieve the required power levels. Unfortunately, secondary gas/plasma is often generated in the system when using this type of cathode. As a consequence, pulse shortening becomes more pronounced, making it difficult to achieve serial shots without severe degradation of the vacuum. It is therefore highly desirable to develop new cathode technologies

that can deliver sufficient current levels in each shot. Some of the considered alternatives are **novel thermionic cathodes** where the heating is done through electron bombardement using lasers[37], **plasma cathodes** where the electron beam is produced from an ionized volume of gas [39], and **ferroelectric cathodes** where one utilizes materials that go through hysteresis during polarization [45].

3. **Improved breakdown prevention for HPM surfaces and windows:** New materials must be developed that can better handle high electric field stresses in confined geometries, large currents, and the presence of X-rays. This can then contribute to reducing the problem of field breakdown. The demands on such materials become more severe as one try to make devices increasingly more compact. Another, more theoretical problem, is the issue of field breakdown near the source window, both internally and externally, when the generated radiation is delivered to the outside world. It is also an issue of how to design compact antennas that are capable of transmitting power levels in the multi-gigawatt range. New numerical methods are needed in order to study the coupling between the locally very strong electromagnetic field and a high-density, weakly ionized gas (air).

4. **Pulsed power:** The design of HPM devices for practical, military use will be governed by the need for compact, lightweight, and not the least, environmentally safe sources. It is therefore essential to reduce both the weight and size of the subsystem providing the initial pulse current. Additional questions are concerned with topics such as pulse lengths and repetition rates.

5. **Computational modelling:** Great progress in HPM research in recent years is due to improved numerical tools such as **Particle-In-Cell (PIC)** [14] and **parametric codes** (see e.g. in [4, 25]) and increased computer resources available. A major challenge facing codes of either methods is the need for sophisticated boundary conditions [79, 82]. The problem is that boundary conditions currently used often are based on semi-analytic models that are only accurate within a limited parameter interval. Another problem is related to the fact that accurate, three-dimensional PIC simulations are computationally very intensive. Small changes in the underlying algorithms can potentially give substantial improvements in the efficiency, and thus expand the range of problems that can be studied numerically using PIC. Parametric codes are today much faster than PIC codes. However codes of this type have so far suffered from the lack of algorithm that are accurate enough. As a consequence, PIC has so far been the dominating method for studying HPM sources and a great varity of codes have been developed (e.g. [18, 42, 80]). The method is also well-known from other areas of plasma physics [16, 17].

6. **Advanced diagnostics:** To better study e.g. phenomena linked to pulse shortening, more accurate methods for measuring both field strengths and polarization, as well as plasma distribution (position and velocity) inside a vacuum tube.

7. **Recirculation of spent beam energy:** Conventional microwave tubes often utilize so-called “depressed collectors”, electron beam collectors maintained at a lower potential relative to

the potential of the beam. This technology makes it possible to recirculate part of the energy used for accelerating the electrons. As a by-product, the electrons hit the collector plate with reduced kinetic energy, which in turn leads to reduced heating of the collector. This is particularly important in HPM devices where heating and spontaneous plasma generation is a problem.

8. **Smart, adaptive HPM devices:** So far, microwave devices have not been equipped with computers to monitor or adjust relevant parameters, which is the case with many other commercial products and appliances. If an HPM device could be controlled via a computer, adjustments to the initial parameters could be done continuously to secure the best possible effect, for instance during serial shots.

9. **Mode conversion:** Many HPM devices generate waves in the circularly polarized TM_{01} waveguide mode. For certain applications, it would be desirable to convert this into the circularly polarized TE_{11} mode or the rectangularly polarized TE_{10} mode. The latter option could for instance make it possible to use standard antenna design for mounting on aircrafts. The mode converters should of course be highly efficient $(> 95\%)$ [81].

10. **Use of permanent magnetic focusing:** When comparing the efficiency of different HPM devices, it is common to ignore the energy requirements for the confining magnetic field that most such devices require. Many of these magnetic field-producing systems can consume more energy and be larger in size and volume than the actual HPM sources themselves. An alternative to current-generated magnetic fields is permanent magnets. This alternative will often result in smaller HPM devices that do not require additional energy for generating the magnetic field. The drawbacks of this alternative are relatively large production costs and large weight.

In addition to the topics listed above, the development of completely new HPM concepts is still an important area of research. Candidates pointed to in [9] is devices based on parallel coupling of several radiation sources [56], klystron devices with multiple electron beams [12], alternatively configured electron beams e.g. sheet beam sources [11], Cerenkov systems operating at frequencies above 30 GHz [65], klystron systems operating at frequencies around 100 GHz [15] and new vircator configurations [29, 36, 47].

10 Solid-state switches: An alternative to vacuum tubes

So far we have focused our attention on vacuum tube technology for producing microwave radiation. However, there is an alternative, namely solid-state microwave devices. In this section we will briefly discuss this alternative, how it is typically operated, and how its performance compares to vacuum tube technology.

All microwave generators convert kinetic energy of an electron stream into coherent electromagnetic radiation. In solid-state devices, the electron stream is sustained by applying a voltage between the emitter and collector electrodes (bipolar junction transistor, **BJT**) or the source and the drain electrodes (field effect transistor, **FET**). The electron stream drifts diffusively through a semiconducting medium. As a consequence, a considerable amount of kinetic energy is converted into heat through collisions with the atoms in the semi-conductor lattice. Long-term exposure to elevated device temperatures (e.g. above $200\,^{\circ}\mathrm{C}$) or ionizing radiation causes degradation of the device operation. Elevated temperatures is particularly critical to operating performance at high frequencies because the mobility of the electrons is reduced. To keep the operating temperature at an acceptable level, the cooling efficiency must be increased by increasing the size of the thermal baseplate. In fact, the size of a solid-state device is typically dominated by the required size of its thermal baseplate and cooling system. An important area of research is therefore to try develop wide bandgap semi-conductors that can operate at higher junction temperatures.

Based on the above discussion, the following advantages of vacuum devices over solid-state devices are listed in [8]:

- Heat production is better separated from the region of wave generation. It is therefore easier to construct solutions for reusing waste energy.
- High output power can be achieved at a higher operating temperature and in environments exposed to ionizing radiation (e.g. upper atmosphere).
- Larger ratios between peak power and average power can be achieved.
- Higher breakdown limits on the maximum $\boldsymbol{E}$-field strength inside the device.
- As a consequence of both reduced heat generation and increased temperature limit for efficient operation, a smaller baseplate or “heatsink” can be used. This will in general lead to smaller devices.

There are however other characteristic properties that can be said to favour the solid-state approach over the vacuum approach. Advantages of the solid-state devices listed in [8] are:

- A capability for very large bandwidths at frequencies below 1GHz.
- Basic devices are typically straightforward to manufacture. This does not include heat reduction systems for high power applications.
- Designing microwave power amplifiers by combining many low-power microwave transistors can be a cost-effective approach to high power generation.
- Typical noise level is lower for solid-state devices (rouhly 2-5 dB) than for vacuum tubes (roughly 20-40 dB for TWTs).

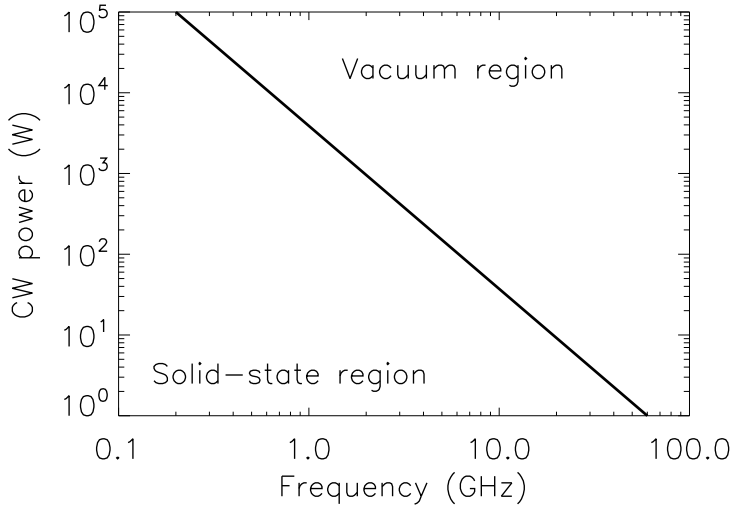

Figure 10.1: Frequency and continuous wave power parameter space has been divided into a solid-state and vacuum tube regime where the corresponding technology normally would be considered to be the most cost-effective approach.

Figure 10.1 illustrates the regimes where each of the two types of microwave devices are normally considered to be the superior alternative. For low-power, low-frequency applications, solid-state devices have justifiably replaced vacuum devices as the dominating technology. However, for high-power, high-frequency application, vacuum tubes still seem to have the upper hand when taking into account peak power, efficiency, and reliability. Only by combining a relatively large number of units, can solid-state devices today deliver adequate power levels at frequencies around 1GHz or higher.

An alternative to choosing either a solid state amplifier or a vacuum tube amplifier is to combined the two approaches into what is known as a **Microwave Power Module (MPM)** [75]. Devices of this kind has been shown to deliver record high continous wave RF power densities due to the incredibly small device volumes and weight, e.g. 200 cm^3 and $0.5-1.0$ kg. The solid-state amplifier in this setting serves as a front-end amplifier for the vacuum tube amplifier. Challenges related to constructing large arrays of MPMs are issues related to device packaging and costs.

11 Conclusion

The first, reasonably efficient, experiments to produce high power microwave radiation were conducted in Russia in 1973 using relativistic BWOs [51]. Motivated by visions of future, technologically advanced, military programs such as the “Star Wars” program, this new branch of MVED (**Microwave Vacuum Electronic Device**) technology grew into a considerable R & D activity dur-

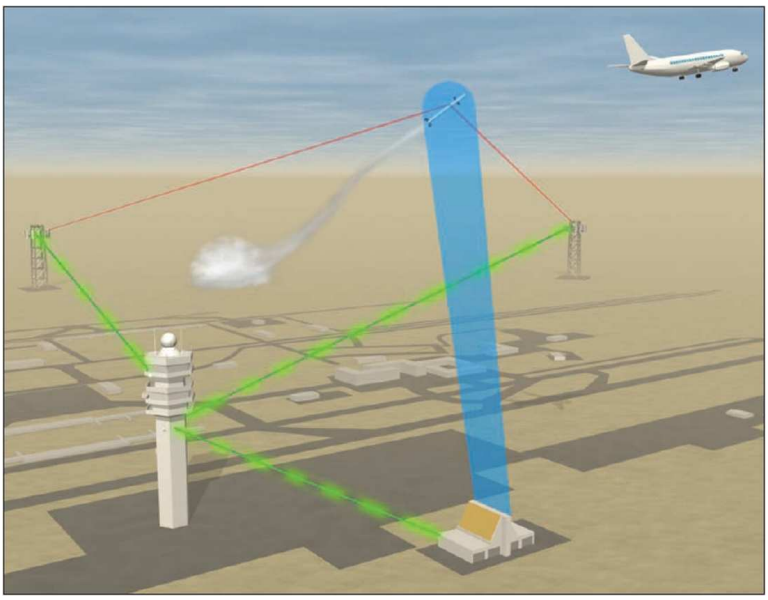

Figure 11.1: Raytheon's **Vigilant Eagle** *system uses high-power microwave pulses to confuse or damage the electronics of shoulder-fired antiaircraft missiles pursuing aircrafts operating from commercial airfields [35].*

ing the 1980s. This new research trend, pushed forward by plasma physicists not too concerned with or skilled in the engineering aspect of the problem, was however not well received by the existing MVED community, dominated by experienced electrical engineers. The division of the MVED community into a large "radar" branch and a smaller "HPM" branch still exists to some extent. Developers of HPM systems have just fairly recently started to realize the great importance of drawing from the long experience and in-depth know-how of MVED production found within the traditional MVED community. This is perhaps one of the main reasons three decades of research on HPM weaponry has not yet resulted in a major breakthrough for this kind of weapons.

The question is whether this means that HPM weapons will never become an important part of military operations of the future. The ongoing research activity in this area indicates that many people working with weapons R & D still see a major potential in HPM. Industry has started to take an interest in the development of HPM weapons offering weaponry ranging from suitcase-sized anti-terror systems [84] to large-scale airport protection systems (see figure 11.1) [35]. HPM weapons on UAV-platforms is another area of strategic importance where commercial companies are now involved [10]. So what general factors point in the direction of a range of tactically deployable HPM weapons becoming a reality within the next 10-15 years ? We will try briefly to answer this question here, leaving a more in-depth discussion of the military potential of HPM technology to a separate report. We will also try to point to what we consider to be the most promising vacuum tube technologies.

11.1 Current state in HPM research

In order to achieve goals in science and technology that requires more than a couple of years development, the degree of success will depend on several factors. Most notably, one needs to have the necessary skills and background to tackle the tasks, one must be sufficiently motivated, and one needs to have adequate tools and resources to do it. We believe that all of these three vital components currently exist in the HPM research today.

1. **Background:** Three decades of basic research on HPM sources has given a good foundation for moving into the engineering phase of the development. It has also become more common to look at how developments in HPM weapons can benefit from developments in radar systems and vice versa. This applies in particular to the development of **active electronically scanned array (ASEA)** radars and to what extent they can be expanded to include weapons effects [34]. At the same time, technological advances have been made in areas that HPM weapons systems might depend heavily on. This includes the development of high energy density capacitors, compact solid-state switches, compact pulsed power modulators, and all-electric platforms.

2. **Motivation:** The last couple of decades have seen a dramatic increase in our dependence on sensitive electronic equipment. This trend will only continue in the years to come as wireless communcations systems move into the battlefield. The potential gain from exposing military or civilian equipment to high power microwave radiation will most problably be high for all foreseeable future. It is therefore reasonble to assume that the research effort on HPM weapons will continue on a substantial level in the years to come.

3. **Computing tools:** Recently, computers have become available that are powerful enough to handle accurate, three-dimensional simulations of HPM devices. This has meant a new era for microwave tube design through so-called **virtual prototyping** [68]. Fast computers will also be important in developing multi-tube systems for increased power and “smart tubes” that can optimize the effect on the intended target [1].

Based on these factors, we believe it is likely that a range of HPM weapons will become a reality within the next 10-15 years.

11.2 Near-future scenarios

Technologies to be used in a military setting will typically be judged not only by the performance in terms of peak RF power produced, pulse length and radiation frequency. Equally important is the size, weight, flexibility, and reliability of the systems. Figure 11.2 shows how the field strength will vary as a function of distance from 3 hypothetical source emitting radiation at the 2GHz frequency. The calculations are based on a simplified far field model with negligible attenuation due to air

propagation [71]. Likewise, it is assumed that the near-field is below the ciritical level for air breakdown. In the graph, three different field levels are indicated, level A (100-1000 V/m), level B (1-20 kV/m), and level C (>20 kV/m). These levels are meant to indicate different regimes for effects on unshielded targets. A level A field strength will typically be sufficient to disturb and in some case damage through front-door coupling, that is via a target antenna, provided the frequency is well-mathced to the intended target [6, 38, 71]. Back-door disturbances is also possible as one gets closer to the 1kV/m limit. In addition to the effects reported on level A, level B field strengths have been reported to effectively stop vehicles [7], shut down or even in some cases permanently damage computers and computer network components [5]. Field strengths of level C would typically lead to permanent damage on unshielded equipment through both front- and back-door coupling.

The smallest source shown in figure 11.2 (solid line) is a 1GW highly compact source. The antenna is assumed to be circular with a radius of 0.5m, resulting in an estimated gain of 26 dB. This system could probably be mounted on smaller patrol vehicles or installed in a casing as a mobile unit. We see from the graph that level C effects will only be obtained at the limited range of 150-200m. However, levels B effects should be observable at distances as large as 3500m. Such a source could therefore be effective in a wide range of small-scale applications. The mid-size source shown in figure 11.2 (dotted line) is a 4GW source with a 1m radius and 32dB gain antenna. This system could be mounted on larger vehicles, such as trucks. Medium-sized ships and airplanes could also be possible carriers. From the graph we see that level C field strengths can be expected upto 600-700m and level B field strengths upto 13-14km. The largest source shown in figure 11.2 is meant to be 16GW multi-source system with a 2m radius and 38 dB gain antenna for larger ships and airplanes. In this case we see that level C field strengths are experienced more than 2.5km away from the source. Even at 10km, the field strength will be more than 5kV/m. Even if we were to take into account moderate attenuation due to atmospheric vapour, we expect the field strength at 30km to be more than 1kV/m. This would represent a powerful directed energy weapon (DEW).

11.3 Most promising HPM source technology

In connection with the 3 different DEW scenarios just described, it is appropriate to ask which HPM source technologies will most likely be used to produce the RF radiation. Devices that require an externally applied magnetic field will typically be larger and either require a more powerful energy source (electrically generated magnetic fields) or have a larger weight and production cost (magnetic fields from permanently magnetic materials). Of the few devices that do not require an externally applied magnetic field is the vircator, the reltron, and the MILO. These systems can all be foreseen as part of mobile units. However, it is difficult to assess exactly what these three devices currently can deliver in terms of RF power and energy when put into an optimal weapons design. The last scientific papers on the reltron were published about a decade ago [61]. The near-future estimates then was that the reltron should be able to deliver RF energy levels of 1-4 kJ per pulse (e.g. 1-2GW power for 1-2μs) with a repetition rate of upto 100Hz. Even though the more optimistic prognosis might not have materialized, it is likely that the reltron tube today can deliver

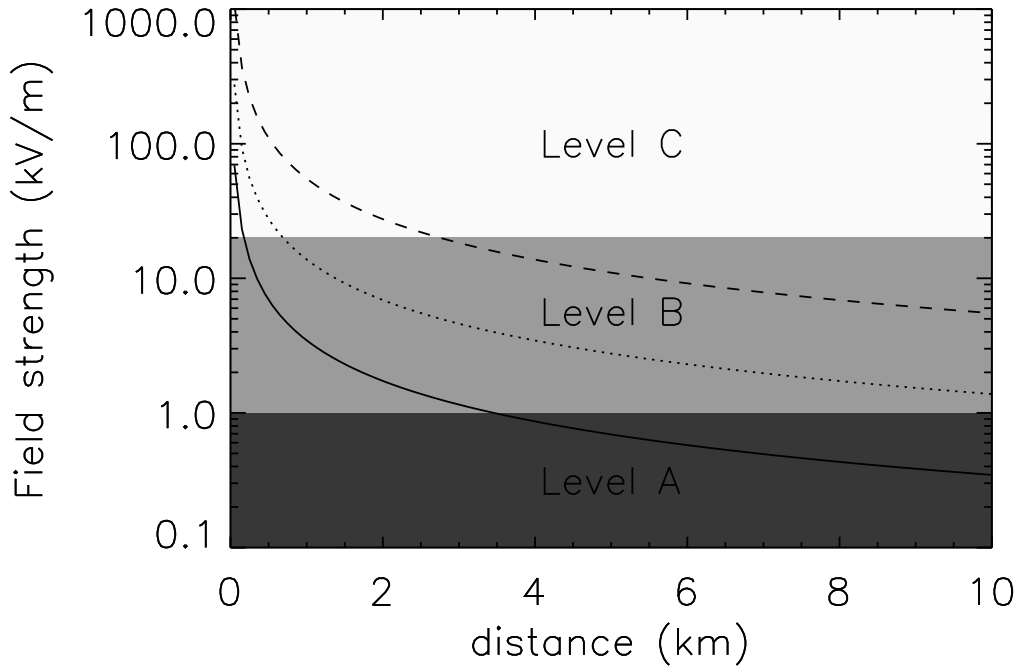

Figure 11.2:

1kJ per pulse with a repetition rate of 10-20Hz. Currently, more modest versions of the device are commercially available from the Titan Corporation [69].

The research on the MILO was initiated in the USA. Again, the unrestricted publication of research results was terminated around a decade ago [43]. At that time, issues regarding anode plasma formation causing pulse shortening was studied. Some papers from the US MILO research were published in 2000/2001 indicating possible solutions to these problems, but the information in these later papers have clearly been made less specific [44]. Based on the information given in the last few US MILO papers, it is reasonable to assume that US MILO devices have produced RF energy levels well over 1kJ per pulse (e. g. 2-3GW for 0.5-1μs). What they have achieved in terms repetition rates is more uncertain. In addition, both the Chinese and the Koreans have had solid MILO programs running over the last decade. This has for instance resulted in improvements on the MILO efficiency by introducing movable parts [31]. The Chinese MILO is also reported to be higly compact with diameter of 26cm and a tube length of 70cm. So far, the experiments reported from these two countries have not included powerful enough pulsed power systems to really study the behaviour of long pulses [31, 48]. However, a numerical study of the Chinese model estimates power levels around 4GW and an efficiency of around 12%.

The technology of the vircator has needed more time to mature than what is the case with the reltron and the MILO. This has to do with the low efficiency of the original vircator designs. In recent years,

the reflex triode has shown promising efficiency levels [47, 57], around 10%. Once again, it seems like the Chinese are dominating the list of publications in recent years. There is even evidence of some collaborations going on between the USA and China on the vircator research. So far, the reflex triode has been reported to produce roughly 200ns pulses with around 500MW of power. Assuming the efficiency is not significantly reduced when increasing the pulsed power, results comparable to that of the reltron and the MILO should already be possible.

Gradually, information on the research on HPM sources is becoming harder to obtain. However, the papers that have been published in recent years indicate that progress is being made. The reason for the reduced amount of information is therefore most likely an indication that HPM source development is leaving the purely academic arena and entering the engineering and commercial arena. It will still take some years before HPM based weapons will find its natural place in military settings. Weapons of this kind depend on a variety of technologies, not only the HPM source itself. Research in the years to come will therefore focus on the supporting technologies rather than on the HPM sources themselves.

References

[1] Abdallah, C. T., Soualian, V. S. & Schamiloglu, E.: **Toward "Smart Tubes" Using Iterative Learning Control**, IEEE Trans. Plasma Sci., 905, 26, 1998

[2] Abramowitz, M. & Stegun, I. A.: **Handbook of Mathematical Functions (5th edition)**, Dover Publications, New York, 1968

[3] Allen, M. A.: **Recent progress in relativistic klystron amplifiers**, Standford Linear Accelerator Center Pub., no. 5070 (Aug.), 1989

[4] Antonsen, T. M. & Levush, B.: **CHRISTINE: A multi-frequency parametric simulation code for traveling wave tube amplifiers**, NRL/FR/6840-97-9845, 1997

[5] Arnesen, O. H.: **High Power Microwave Trials 11-13 May 2004. Results from tests on Local Area Network**, FFI/RAPPORT-2004/03958, 2004

[6] Bäckström, M. G. & Lövstrand, K. G.: **Susceptibility of Electronic Systems to HPMs: Summary og Test Experience**, IEEE Trans. Electromagnetic Compatibility, 396, 46, 2004

[7] Bäckström, M. G.: **Testing of a car's immunity againt high intensity pulsed microwaves**(in Swedish), FOA-R–95-00099–SE, 1995

[8] Barker, R. J. et al. (Eds.): **Modern Microwave and Millimeter-wave Power Electronics**, IEEE Press, New York, 2005

[9] Barker, R. J. & Schamiloglu, E. (Eds.): **High-Power Microwave Sources and Technologies**, IEEE Press, New York, 2001

[10] Barrie, D.: **Focused Effort**, Aviation Week & Space Tech., 39/8, 167, 2007

[11] Basten, M. A. & Booske: **Two-plane Focusing of High-Space-Charge Sheet Electron Beams using Periodically-cusped Magnetic Fields**, J. Appl. Phys. 6313, 8, 1999

[12] Bearzatto, C., Beunas, A. & Faillon, G.: **Long Pulse and Large Bandwidth Mulitbeam Klystron**, Proc. AIP Conf., ed. R. M. Phillips, 107, 474, 1998

[13] Benford, J. & Swegle, J.: **High Power Microwaves**, Artech House, Norwood, 1991

[14] Birdsall, C. K. & Langdon, A. B.: Plasma Physics via Computer Simulation, McGraw-Hill, New York, 1985

[15] Blank, M. et al.: **Deonstration of a 10kW average power 94GHz gyroklystron amplifier**, Phys. Plasmas, 4405, 6, 1999

[16] Børve, S.: **Particle Simulation for Plasma in 2.5D for Phenomena on the Ion Plasma Period Time Scale** Masters Thesis, University of Oslo, Oslo, 1998

[17] Børve, S., Pécseli, H. L. & Trulsen, J.: **Ion phase-space vortices in 2.5-dimensional simulations**, J. Plasma Phys., 107, 65, 2001

[18] Botton, M. et al.: **MAGY: A Time Dependent Code for Simulation of Electron beam Devices**, IEEE Trans. Plasma Sci., 882, 26, 1998

[19] Briggs, R. J.: **Space-charge waves on a relativistic, unneutralized electron beam and collective ion acceleration**, Phys. Fluids, 1257, 19, 1976

[20] Bugaev, S. P. et al.: **Investigation of a Millimeter-Wavelength-Range Relativistic Diffraction Generator**, IEEE Trans. Plasma Sci., 518, 18, 1990

[21] Bugaev, S. P. et al.: **Relativistic Multiwave Cerenkov Generators**, IEEE Trans. Plasma Sci., 525, 18, 1990

[22] Carlsten, B. E. et al.: **Intense Space-Charge Beam Physics Relevant to Relativistic Klystron Amplifiers**, IEEE Trans. Plasma Sci., 719, 22, 1994

[23] Choi, S. H., Schamiloglu, E. & Miller, R. B.: **Initial operation of an ultra-compact, low voltage reltron microwave source**, Pulsed Power Plasma Science, IEEE Conference, Las Vegas, 2001

[24] Chu, K. R.: **The electron cyclotron maser**, Rev. Modern Phys., 489, 76, 2004

[25] Cooke, S. et al.: **CTLSS – An advanced Electromagnetic Simulation Tool for Designing high-Power Microwave Sources**, IEEE Trans. Plasma Sci., 841, 28, 2000

[26] Cousin, R.: **Compréhension des mécanismes régissant le functionnement d'un tube hyperfréquence de type MILO**, L'Ecole Polytechnique, Palaiseau Cedex, France, 2005

[27] Davies, H. A., Fulton, R. D., Sherwood, E. G. & Kwan, T. J. T.: **Enhanced-Efficiency, Narrow-Band Gigawatt Microwave Output of the Reditron Oscillator**, IEEE Trans. Plasma Sci., 611, 18, 1990

[28] Davidson, R. C., Chan, H.-W., Chen, C. & Lund, S.: **Equilibrium and stability properties of intense non-neutral electron flow**, Rev. Mod. Phys., 341, 63, 1991

[29] Didenko, A. N., Zherlitsyn, A. G. & Melnikow, G. V.: **Research of Microwave Generation Efficiency for Triode with Virtual Cathode (Vircator Triode)**, Proc. 12th Int. Conf. on High Power Particle Beams, 65, 1998

[30] Elfsberg, M., Appelgren, P., & Hultman, T.: **Beskrivning av och inledande försök med ett system bestående av laddaggregat och marxgenerator**, FOI-R–1202–SE, 2004

[31] Fan, Y.-W. et al.: **A Compact Magnetically Insulated Line Oscillator with New-Type Beam Dump**, Chin. Phys. Lett., 164, 22, 2005

[32] Fan, Y.-W. et al.: **Simulation Investigation of an Improved MILO**, IEEE Trans. Plasma Sci., 379, 35, 2007
bibitemfly88 Flyagin, V. A. & Nusinovich, G. S.: **Gyrotron Oscillators**, Proc. IEEE, 644, 76, 1988

[33] Forsvarsbygg: **Elektromagnetiske Våpen, Håndbok i våpenvirkninger**, Forsvarsbygg, Oslo, 2003

[34] Fulghum, D. A.: **Weapon Concerns**, Aviation Week Space Tech., 72/12, 164, 2006

[35] Fulghum, D. A.: , Aviation Week Space Tech., 116/24, 162, 2005

[36] Gadetskii, N. P. et al.: **The Virtode: a Generator Using Supercritical REB Current with Controlled Feedback** Plasma Phys. Rep., 273, 19, 1993

[37] Gärtner, G., Geittner, P., Lydtin, H. & Ritz, A.: **Emission Properties of Top-layer Scandate Cathodes Prepared by LAD**, Appl. Surf. Sci. 11, 111, 1997

[38] Giri, D. V. & Tesche, F. M.: **Classification of Intentional Electromagnetic Environments (IEME)**, IEEE Trans. Electromagnetic Compatibility, 322, 46, 2004

[39] Goebel, D. M., Schumacher, R. W. & Watkins, R. M.: **Long-pulse Plasma Cathode E-gun**, Proc. 9th Int. Conf. High Power Particle Beams, 1093, 1992

[40] Goldstein, R. J. & Rutherford, P. H.: **Plasma Physics**, IOP Publishing,, London, 1995

[41] Gomberoff, K. & Deutsch, A.: **Particle-In-Cell Simulation of a Grounded Cathode Magnetron**, IEEE Trans. Plasma Sci., 590, 34, 2006

[42] Goplen, B., Ludeking, L., Smithe, D. & Warren, G.: **User-configurable MAGIC for electromagnetic PIC calculations**, Comp. Phys. Comm., 54, 87, 1995

[43] Haworth, D. et al.: **Significant Pulse-Lengthening in a Multigigawatt Magnetically Insulated Transmission Line Oscillator**, IEEE Trans. Plasma Sci., 312, 26, 1998

[44] Haworth, D. et al.: **Improved Electrostatic Design for MILO Cathodes**, IEEE Trans. Plasma Sci., 992, 30, 2002

[45] Jiang, B., Kirkman, G. & Reinhardt, N.: **High Brightness Electron Beam Produced by a Ferroelectric Cathode**, Appl. Phys. Lett., 1196, 66, 1995

[46] Jiang, W. & Kristiansen, M.: **Theory of the virtual cathode oscillator**, Phys. Plasmas, 3782, 8, 2001

[47] Jiang, W., Shimada, N., Prasad, S. D. & Yatsui, K.: **Experimental and numerical studies of New Configuration of Virtual Cathode Oscillator**, IEEE Trans. Plasma Sci. 54, 32, 2004

[48] Kim, D. H. et al.: **Experimental Investigation of Giga-watt Magnetically Insulated Transmission Line Oscillator (MILO) by Improved Axial Power Extraction**, 7th IEEE Int. Vacuum Electronics Conf., Monterey, 2006

[49] Kopp, C.: **The Electromagnetic Bomb - A Weapon of Electrical Mass Destruction** Air & Space Power J., 1997

[50] Korovin, S. D., Polevin, S. D., Roitman, A. M. & Rostov, V. V.: **Relativistiv Backward Wave Tube with Variable Phase Velocity** Sov. Tech. Phys. Lett., 265, 18, 1992

[51] Kovalev, N. F. et al.: **Generation of powerful electromagnetic radiation pulses by a beam of relativistic electrons** J. Exp. Theor. Phys. Lett., 138, 18, 1973

[52] Krogager, E.: **High Power Microwaves - Measures and Countermeasures**, RTO-MP-SCI-158, 2006

[53] Larsson, A., Appelgren, P., Nylander, C. & Nyholm, S. E.: **narrow-band radiation sources for HPM applications**, FOI-R–0929–SE, 2003

[54] Lau, Y. Y.: **Some design considerations on using modulated intense annular electron beams for particle acceleration**, J. Appl. Phys. 351, 62, 1987

[55] Lau, Y. Y., Friedman, M., Krall, J. & Serlin, V.: **Relativistic Klystron Amplifiers Driven by Modulated Intense Relativistic Electron Beams**, IEEE Trans. Plasma Sci., 553, 18, 1990

[56] Levine, J., Aiello, N., Benford, J. & Harteneck, B.: **Design and Operation of a Module of Phase-locked Relativistic Magnetrons**, J. Appl. Phys., 2838, 70, 1991

[57] Liu, L. et al.: **Efficiency Enhancement of Reflex Triode Virtual Cathode Oscillator Using the Carbon Fiber Cathode**, IEEE Trans. Plasma Sci., 361, 35, 2007

[58] Mahaffey, R. A., Sprangle, P., Golden, J. & Kapetanakos, C. A.: **High-Power Microwaves from a Nonisochronic Reflexing System**, Phys. Rev. Lett., 842, 39, 1977

[59] Miller, R. B., McCullough, W. F., Lancaster, K. T., & Muehlenweg, C. A.: **Super-Reltron Theory and Experiments** IEEE Trans. Plasma Sci., 332, 20, 1992

[60] Miller, R. B., Muehlenweg, C. A., Habiger, K. W. & Clifford, J. R.: **Super-Reltron Progress** IEEE Trans. Plasma Sci., 701, 22, 1994

[61] Miller, R. B.: **Pulse Shortening in High-Peak-Power Reltron Tubes** IEEE Trans. Plasma Sci., 340, 26, 1998

[62] Miller, S. M., Antonsen, Jr., T. M., Levush, B. & Vlasov, A. N.: **Cyclotron Resonances in Relativistic BWOs Operating Near Cutoff** IEEE Trans. Plasma Sci., 859, 24, 1996

[63] Nation, J. A.: **On the Coupling of A High-current Relativistic Beam to a Slow Wave Structure**, Appl. Phys. Lett., 491, 17, 1970

[64] Naqvi, S. A., Nation, J. A., Schächter, L. & Wang, Q.: **High Efficiency TWT Design Using Traveling-wave Bunch Compression**, IEEE Trans. Plasma Sci., 840, 26, 1998

[65] Nusinovich, G. S. et al.: **Recent Progress in the Development of Plasma-filled Traveling-Wave Tubes and Backward-Wave Oscillators**, IEEE Trans. Plasma Sci., 628, 26, 1998

[66] Nylander, C., Hurtig, T., Larsson, A., & Nyholm, S. E.: **Simulering av reflextriod med MAGIC**, FOI-R–1670–SE, 2005

[67] Orzechowski, T. J. et al.: **High-Efficiency Extraction of Microwave Radiation from a Tapered-Wiggler Free-Electron Laser**, Phys. Rev. Lett., 2172, 57, 1986

[68] Peterkin, R. E. & Luginsland, J. W.: **Virtual Prototyping Environment for Directed-Energy Concpets**, Comput. Sci. Eng., 42, 4, 2002

[69] Price, D. et al.: **DEW Technology at the Titan Corporation**, 1st Inter. Energy Conversion Eng. Conf., Portsmouth, USA, 2003

[70] Roberson, C. W. & Sprangle, P.: **A review of free-electron lasers**, Phys. Fluids B, 3, 1, 1989

[71] Serafin, D. J. & Dupouy, D.: **Potential IEMI threat against civilian air traffic**, URSI2005 General Assembly, New Delhi, India, 2005

[72] Swegle, J. A., Poukey, J. W. & Leifeste, G. T.: **Backward wave oscillators with riplled wall resonators: Analytic theory and numerical simulation**, Phys. Fluids, 2882, 28, 1985

[73] Schamiloglu, E., Schoenbach, K. & Vidmar, R.: **Basic Research on Pulsed Power for Narrowband High Power Microwave Source**, Proc. SPIE, Intense Microwave Pulses IX, Orlando, Florida, 1, 2002

[74] Schneider, J.: **Stimulated Emission of Radiation by Relativistic Electrons in a Magnetic Field**, Phys. Rev. Lett., 504, 2, 1959

[75] Smith, C. R., Armstrong, C. M. & Duthie, J.: **The MicrowavePower Module: A Versatile RF Building Block for High-Power Transmitters**

[76] Sprangel, P. & Drobot, A. T. **The Linear and Self-Consistent Nonlinear Theory of Electron Cyclotron Maser Instability**, IEEE Trans. Microwave Theory and Tech., 528, 25, 1977

[77] Sprangel, P., Tang, C. M. & Manheimer, W. M.: **Nonlinear theory of free-electron lasers and efficiency enhancement**, Phys. Rev. A, 302, 21, 1980

[78] Uhm, H. S.: **A Theoretical Analysis of Relativistic Klystron Oscillators**, IEEE Trans. Plasma Sci., 706, 22, 1994

[79] Vahedi, V. & Surendra, M.: **Monte Carlo collision model for particle-in-cell method: Application to argon and oxygen discharges**, Comput. Phys. Commun., 179. 87, 1995

[80] Verboncoeur, J. P., Langdon, A. B. & Gladd, N. T.: **An Object-oriented Electromagnetic PIC Code**, Comp. Phys. Commun., 199, 87, 1995

[81] Vinogradov, D. V. & Denisov, G. G.: **Waveguide Mode Convertors with Step Type Coupling**, Int. J. Infrared and millimeter Waves, 131, 12, 1991

[82] Wang, J., Wang, Y. & Zhang, D.: **Truncation of open Boundaries of Cylindrical Waveguides in 2.5-dimensional Problems by using the Convolutional Perfectly Matched Layer**, IEEE Trans. Plasma Sci., 681, 34, 2006

[83] Webster, D. L.: **Cathode-Ray Bunching**, J. Appl. Phys., 501, 10, 1939

[84] Weise, Th. H. G. G. et al.: **Overview of Directed Energy Weapon Developments**, 12th IEEE Symp. on Electromagnetic Launch Tech., Snowbird, Utah, 2004

[85] Zavjalov, M. A. et al.: **Powerful wideband amplifier based on hybrid plasma-cavity slow-wave structure**, IEEE Trans. Plasma Sci., 600, 22, 1994

A Small-amplitude wave analysis

A common technique in linear wave analysis is to linearize the governing equations by neglecting all terms of higher than first order. To achieve this, all relevant quantities should be expressed as an equilibrium solution with a small-amplitude, wave correction added to that. To be able to illustrate the procedure on a simplified problem, we will make the following assumptions: (1) Fluid velocities are well below the speed of light. Therefore, no relativistic corrections or self-consistent magnetic

fields need to be taken into account. (2) All equilibrium solutions are uniform. (3) All relevant waves propagate in the $z-$direction. (4) The particles are restricted to move parallel to the wave propagation, that is in the $z-$direction. (5) Wave amplitudes are only allowed to vary as a function of $\boldsymbol{r}_\perp$, position perpendicular to the wave propagation. Initally, we will only make the first two assumptions. Later, when all 5 assupmtions are made, the model will be identical to that used in the analysis of space-charge waves in section 3.2.

We will find a linear solution to a system described by equations 2.7, 2.9, and 2.10. All physical variables are expressed on the form

$$f(\boldsymbol{r}) = f_0 + \delta f(\boldsymbol{r}) e^{i(\boldsymbol{k}\cdot\boldsymbol{r} - \omega t)}. \tag{A.1}$$

We will refer to $K = \omega/c$ as the free space wavenumber. Starting with equation 2.7 and assuming the functional form given in equation A.1, we get

$$\boldsymbol{\nabla}^2 \delta\boldsymbol{E} - (k^2 - K^2)\delta\boldsymbol{E} = \epsilon_0^{-1}(i\boldsymbol{k} + \boldsymbol{\nabla})\delta\rho - i\omega\mu_0\delta\boldsymbol{J}. \tag{A.2}$$

Next, we look at the continuity equation, equation 2.9, which in linearized form can be written as

$$-i\omega\delta\rho + (i\boldsymbol{k} + \boldsymbol{\nabla}) \cdot \delta\boldsymbol{J} = 0. \tag{A.3}$$

Finally, the momentum equation, equation 2.10, will in the current context look like

$$[-i\omega + \boldsymbol{v}_0 \cdot (i\boldsymbol{k} + \boldsymbol{\nabla})]\delta\boldsymbol{v} = -\frac{e}{m}\delta\boldsymbol{E}. \tag{A.4}$$

In addition, we need the linearized relation between the amplitudes in current, charge density, and velocity,

$$\delta\boldsymbol{J} = \delta\rho\boldsymbol{v}_0 + \rho_0\delta\boldsymbol{v}, \tag{A.5}$$

to be able to find a dispersion relation.

At this point, we will invoke the last 3 assumptions listed above before trying to find a dispersion relation based on the $z-$component of equation A.2. From equation A.4 we get

$$\delta v_z = -\frac{ie\delta E_z}{m(\omega - v_{0z}k)}. \tag{A.6}$$

By combining equations A.5 and A.6 with equation A.3, we get the following expressions for the charge density and current, respectively:

$$\delta\rho = \frac{k\rho_0}{\omega - v_{0z}k}\delta v_z = \frac{ik\epsilon_0\omega_p^2}{(\omega - v_{0z}k)^2}\delta E_z \tag{A.7}$$

and

$$\delta J_z = \frac{\omega}{k}\delta\rho = \frac{i\omega\epsilon_0\omega_p^2}{(\omega - v_{0z}k)^2}\delta E_z \tag{A.8}$$

where $\omega_p^2 = e^2 n_0/(\epsilon_0 m) = -e\rho_0/(\epsilon_0 m)$ is the electron plasma frequency squared. Inserting equations A.7 and A.8 into the $z-$component of equation A.2, results in the following:

$$\boldsymbol{\nabla}_\perp^2 \delta E_z - (k^2 - K^2)\left[1 - \frac{\omega_p^2}{(\omega - v_{0z}k)^2}\right]\delta E_z = 0. \tag{A.9}$$

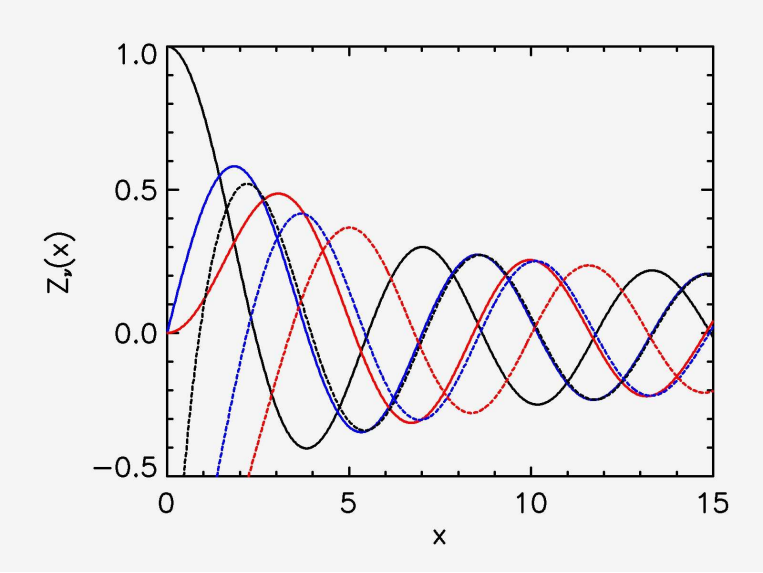

Figure B.1: Bessel functions of the first ($J_\nu(x)$) and second kind ($Y_\nu(x)$) plotted with solid and dotted lines, respectively. The black, blue, and red lines correspond to, in the same order, $\nu = 0, 1, 2$.

B Bessel functions

The Bessel functions are general solutions to the **Bessel's differential equation** that can be written as

$$x^2 \frac{\partial^2 f}{\partial f} \partial x^2 + x \frac{\partial f}{\partial x} + (x^2 - \nu^2) f = 0 \tag{B.1}$$

for an arbitrary real or complex ν. This differential equation, or a variant of it, occurs naturally when solving problems of wave propagation in cylindrical or spherical symmetry. Since equation B.1 is of second order, there exist two linearly independent solutions, known as the first ($J_\nu(x)$) and second ($Y_\nu(x)$) kind Bessel functions of order ν. The former function can be written as

$$J_\nu(x) = \sum_{m=0}^{\infty} \frac{(-1)^m}{m!\Gamma(m+\nu+1)} \left(\frac{x}{2}\right)^{2m+\nu}, \tag{B.2}$$

where

$$\Gamma(x) = \int_1^\infty e^{-t} t^{x-1} dt + \sum_{n=0}^{\infty} \frac{(-1)^n}{n!(x+n)} \tag{B.3}$$

is the standard Γ-function. The second kind Bessel function relates to the first kind by the expression

$$Y_\nu(x) = \frac{J_\nu(x)\cos(\nu\pi) - J_{-\nu}(x)}{\sin(\nu\pi)}, \tag{B.4}$$

which in case of ν being an integer must be evaluated by taking the limit. In this case, we can utilize the following two properties

$$Z_{-\nu}(x) = (-1)^\nu Z_\nu(x), \tag{B.5}$$

and

$$\frac{dZ_\nu(x)}{dx} = \pm Z_{\nu\mp1}(x) \mp \frac{\nu}{x} Z_\nu(x), \tag{B.6}$$

where $Z_\nu(x)$ here represent either $J_\nu(x)$ or $Y_\nu(x)$. The property in equation B.6 also implies that

$$\frac{dZ_0(x)}{dx} = -Z_1(x) \tag{B.7}$$

and

$$J_\nu(x)\frac{dY_\nu(x)}{dx} - Y_\nu(x)\frac{dJ_\nu(x)}{dx} = Y_\nu(x)J_{\nu+1}(x) - J_\nu(x)Y_{\nu+1}(x). \tag{B.8}$$

From [2] we have that the expression in equation B.8 equals $2/(\pi x)$. Both Bessel functions are plotted in figure B.1 using solid ($J_\nu(x)$) and dotted ($Y_\nu(x)$) lines, respectively, for ν equals 0 (black), 1 (blue), 2 (red).

If the argument is assumed to be purely imaginary, written as ix where x is real, we get what is known as the **modified Bessel equation**,

$$x^2\frac{\partial^2 f}{\partial f}\partial x^2 + x\frac{\partial f}{\partial x} - (x^2+\nu^2)f = 0. \tag{B.9}$$

The two, linearly independent solutions to equation B.9 are known as the modified Bessel functions of the first ($I_\nu(x)$) and second ($K_\nu(x)$). These functions can be expressed as

$$I_\nu(x) = i^{-\nu}J_\nu(ix) \tag{B.10}$$

and

$$K_\nu(x) = \pi\frac{I_{-\nu}(x) - I_\nu(x)}{2\sin(\nu\pi)}, \tag{B.11}$$

and are plotted in figure B.2.

In the case of spherical, rather than cylindrical, wave propagation, a differential equation similar to

$$x^2\frac{\partial^2 f}{\partial f}\partial x^2 + 2x\frac{\partial f}{\partial x} + [x^2 - \nu(\nu+1))f = 0 \tag{B.12}$$

might occur. This is known as the **spherical Bessel equation**. The solutions are correspondingly named the spherical Bessel functions of the first ($j_\nu(x)$) and second ($y_\nu(x)$) kind. These functions depend on the original Bessel functions through the relations

$$j_\nu(x) = \sqrt{\frac{\pi}{2x}}J_{\nu+1/2}(x) \tag{B.13}$$

and

$$y_\nu(x) = \sqrt{\frac{\pi}{2x}}Y_{\nu+1/2}(x) \tag{B.14}$$

and are plotted in figure B.3.

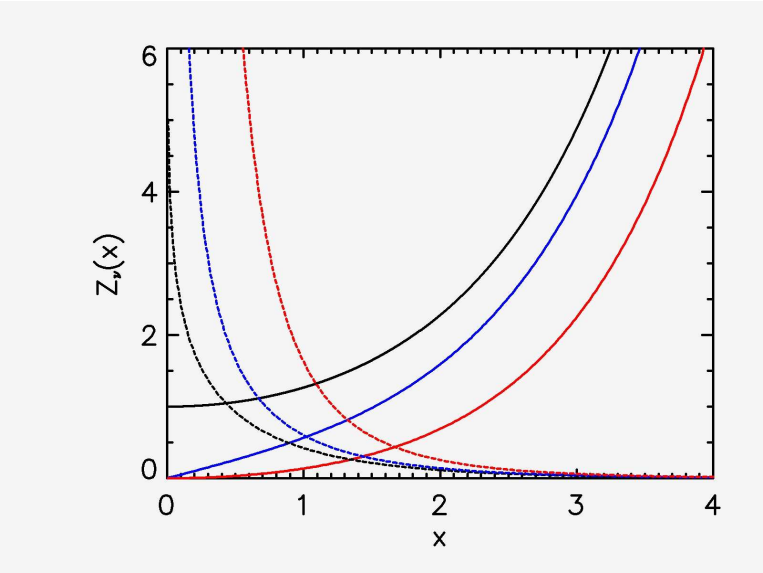

Figure B.2: Modified Bessel functions of the first ($I_\nu(x)$) and second kind ($K_\nu(x)$) plotted with solid and dotted lines, respectively. The black, blue, and red lines correspond to, in the same order, $\nu = 0, 1, 2$.

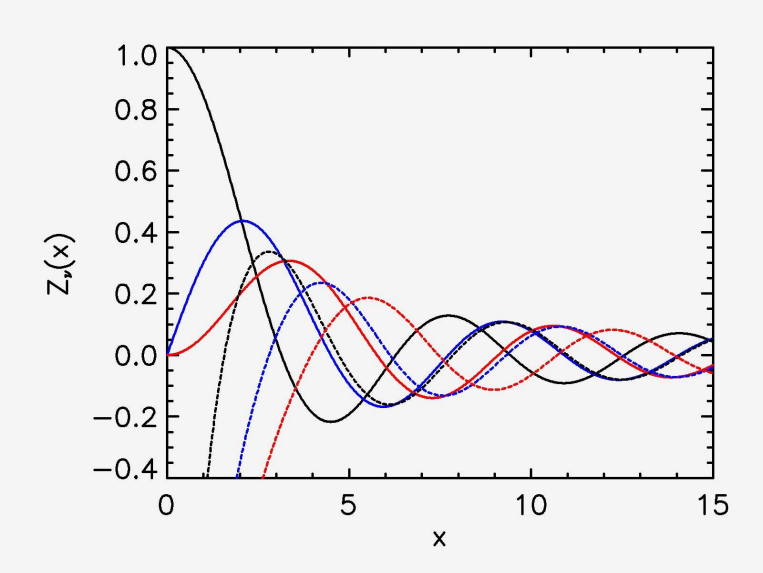

Figure B.3: Spherical Bessel functions of the first ($j_\nu(x)$) and second kind ($y_\nu(x)$) plotted with solid and dotted lines, respectively. The black, blue, and red lines correspond to, in the same order, $\nu = 0, 1, 2$.